

# Planetary Dynamos in Evolving Cold Gas Giants

Albert Elias-López<sup>1,2,7</sup>, Fabio Del Sordo<sup>1,3,4</sup>, Daniele Viganò<sup>1,2,5</sup>, Clàudia Soriano-Guerrero<sup>1,2</sup>, Taner Akgün<sup>1,2</sup>, Alexis Reboul-Salze<sup>6</sup>, Matteo Cantiello<sup>7,8</sup>

<sup>1</sup> Institut de Ciències de l'Espai (ICE-CSIC), Campus UAB, Carrer de Can Magrans s/n, 08193 Cerdanyola del Vallès, Barcelona, Catalonia, Spain

<sup>2</sup> Institut d'Estudis Espacials de Catalunya (IEEC), 08860 Castelldefels, Barcelona, Catalonia, Spain

<sup>3</sup> INAF, Osservatorio Astrofisico di Catania, via Santa Sofia, 78 Catania, Italy

<sup>4</sup> Scuola Normale Superiore, Piazza dei Cavalieri, 7 56126 Pisa, Italy

<sup>5</sup> Institute of Applied Computing & Community Code (IAC3), University of the Balearic Islands, Palma, 07122, Spain

<sup>6</sup> Max Planck Institute for Gravitational Physics (Albert Einstein Institute), D-14476 Potsdam, Germany

<sup>7</sup> Center for Computational Astrophysics, Flatiron Institute, 162 5th Avenue, New York, NY 10010, USA

<sup>8</sup> Department of Astrophysical Sciences, Princeton University, Princeton, NJ 08544, USA

e-mail: albert.elias@csic.es

Received ———; accepted ———

## ABSTRACT

*Context.* The discovery of thousands of exoplanets has started a new era of planetary science, expanding our ability to characterize diverse planetary features. However, magnetic fields remain one of the least understood aspects of exoplanetary systems. A deeper understanding of planetary dynamos and the evolution of surface magnetic properties throughout a planet's lifetime is a key scientific purpose, with implications for planetary evolution, habitability, and atmospheric dynamics.

*Aims.* This study models the evolution of magnetic fields generated by dynamo action in cold giant gaseous planets. We aim to explore how the topology and strength of magnetic fields change across different evolutionary stages, providing a comprehensive view of their lifecycle.

*Methods.* We solve the resistive magnetohydrodynamic (MHD) equations under anelastic approximation with a 3D pseudo-spectral spherical shell MHD code. We employ 1D thermodynamical hydrostatic profiles taken from gas giant evolutionary models as the background states of our MHD models. Numerical integration leads to saturated dynamo solutions. Such calculations are performed with radial profiles corresponding to different planetary ages so that we can interpret them as different snapshots of the magnetoconvection evolution during the long-term planetary evolution.

*Results.* We characterize magnetic fields at different stages of a cold gaseous planet's evolution. We find the occurrence of a transition from multipolar to dipolar-dominated dynamo regime throughout the life of a Jovian planet. During the planetary evolution and the cooling down phase, we observe a decrease in the average magnetic field strength near the dynamo surface as  $\sim t^{-0.2} - t^{-0.3}$ , a trend compatible with previously proposed scaling laws. We also find that some dimensionless parameters evolve differently for the multipolar to dipolar branch, possibly reflecting a force balance change.

*Conclusions.* Our method captures the long-term evolution of the internal dynamo phases of magnetic fields by considering snapshots at different ages, finding a slow decay and a transition in dynamo behavior. This approach can be extended to study hot gaseous planets, offering a versatile tool for interpreting the magnetic properties of giant planets.

**Key words.** planetary dynamos – anelastic approximation – gigayear evolution – cold gas giants

## 1. Introduction

During the last decades, many numerical solutions to the magnetohydrodynamic (MHD) equations in convective spherical shells have been obtained under various assumptions and parameters. Simulations of this type produce amplification and self-sustaining of magnetic fields which can recover some observed aspects related to planetary dynamo in gas giants, such as magnetic field topology or the latitudinal variations of the atmospheric jets (Jones 2011; Schubert & Soderlund 2011, e.g.). High-resolution models are getting closer to reproducing Earth and Jupiter's internal dynamos (Schaeffer et al. (2017); Gastine & Wicht (2021), respectively), including stochastic dipole reversals resembling the geomagnetic field (Glatzmaier & Coe 2007). In planetary science, MHD equations are typically expressed using dimensionless dynamo numbers: Rayleigh, Ekman, Prandtl, and magnetic Prandtl numbers, or combinations thereof. These numbers quantify the relative influence of

various fluid forces such as dissipative, buoyant, and Coriolis forces. There is an unavoidable computational caveat: the parameter space accessible through numerical simulations diverges significantly from physical reality, with some parameters (Rayleigh and Ekman in particular) diverging by many orders of magnitude. This is because the relevant spatial scales to be followed span too wide of a range, i.e. from the microscopical diffusion to the planetary scale for the global rotation or convection patterns.

To partially surpass this intrinsic drawback, some studies have used many numerical models to find scaling laws between different dynamo numbers. For example, for rapidly rotating dipole-dominated dynamo solutions under the Boussinesq approximation, Christensen & Aubert (2006) derived scaling laws that connect the dynamo parameters spanning at least two orders of magnitude. These relations should also arguably work in the real planetary regime, as the relative importance of each term in the

Navier-Stokes equation (the force balance) is expected to be similar to numerical models (Davidson 2013; Yadav et al. 2016).

For gas giant modeling, the anelastic approximation (e.g. Braginsky & Roberts 1995; Gilman & Glatzmaier 1981; Glatzmaier 1984, 1985a,b; Lantz & Fan 1999) is more appropriate than the Boussinesq approximation, as it allows for density variations but still effectively filters out the sound and magneto-sonic waves. It relies on using a static, adiabatic, and spherically symmetric background reference state, specified by density, gravity, temperature, and other thermodynamic variables. On top of it, the velocity and magnetic fields are evolved together with the deviations from the background. These equations have been extensively used to model the magnetic field of gas giants and stars. Usually, the no-slip boundary conditions used by geodynamo models are replaced by stress-free ones, as they better reflect the nature of the gas giant outer atmosphere. The simulations are more computationally demanding, and the numerical solutions have several features that are not seen in the Boussinesq approximation. For example, they often show competition between the development of Jupiter-like zonal flows, which promote weaker multipolar fields, and strong dipole fields, which can suppress such zonal flows via Lorentz forces (e.g. Grote et al. 2000; Simitev & Busse 2003, 2009; Sasaki et al. 2011; Schriener et al. 2012; Duarte et al. 2018). Another example is the bistability found for not too large Rayleigh numbers: both dipolar-dominated and multipolar solutions coexist with identical parameters (Gastine et al. 2012), where different solutions can be reached by setting different initial conditions (Schriener et al. 2012). In this context, Yadav et al. (2013) provided scaling laws for dynamo models under anelastic approximation similar to those of Christensen & Aubert (2006). In this case, both dipolar and multipolar solutions as well as a different range of density stratification and radial-dependent diffusivities were used.

For more realistic gas giant modeling, the challenge is to incorporate the outer steep gradients of various thermodynamical profiles, since they imply very different timescales as one moves outwards. Moreover, there is a steep outward decrease in electrical conductivity due to the hydrogen not being in the metallic state in the outer planetary layers. This behavior was quantified along the Jovian adiabat by French et al. (2012) and has been used during the last decade in different dynamo simulations (Gastine & Wicht 2012; Jones 2014; Gastine et al. 2014; Wicht et al. 2019b). These studies provide important results in terms of comparison with the data provided by the ongoing Juno mission and earlier Jovian missions, highlighting the importance of incorporating a realistic background, although of course with the caveat on the dynamo numbers mentioned above. In recent years, some works (Gastine & Wicht 2021; Yadav et al. 2022) have added a stably stratified layer just below the region where metallic hydrogen starts mimicking a helium rain region due to hydrogen-helium de-mixing (Klepeis et al. 1991; Nettelmann 2015; Nettelmann et al. 2015). This layer helps to naturally get alternating east-west zonal winds centered around the equator for the Jovian dynamo as well as a highly axisymmetric magnetic field for the Saturn model.

By using the aforementioned scaling laws as well as observations, Christensen et al. (2009) determined that for both planets and fast-rotating stars, it is the energy flux that determines the magnetic field strength. To match observational constraints, Reiners et al. (2009) expressed this law in

terms of the mass  $M$ , luminosity  $L$ , and radius  $R$  in a more simplified form. Using this scaling law and the analytical evolutionary tracks for sub-stellar objects in (Burrows & Liebert 1993; Burrows et al. 2001), Reiners & Christensen (2010) provided a magnetic field evolution scenario obtaining a steady weakening (a factor of  $\sim 10$  over around 10 Gyr) of the magnetic field at the dynamo surface.

In this work, we aim to address the long-term evolution of the dynamo action in Jupiter-like planets through an alternative approach. We perform 3D anelastic dynamo simulations with a background corresponding to different ages of the long-term planetary evolution. By comparing how the solutions change from one age to another, and keeping in mind the intrinsic caveats related to the accessible ranges of dynamo numbers, we evaluate the trend in topology and intensity changes that an internal dynamo in cold gas giants can undergo during its Gyr evolution.

This work is organized as follows: the overall methodology and the internal thermodynamical profiles coming from the evolutionary code MESA are described in §2, where we also summarize our 3D dynamo models, performed with the MagIC code<sup>1</sup>; in §3 we show the main results of our parameter exploration, we interpret simulations representative of different evolutionary stages, and we compare these results from other works; finally, we conclude §4.

## 2. Methodology

Simulating the realistic time evolution of the radial dependency of thermodynamic quantities of a 3D magnetoconvection planetary environment is not currently feasible. The main reason is that the timescale associated with internal gas giant planetary convection tends to be of the order of years or decades, while the planetary secular cooling and contraction are appreciable at timescales of the order of giga-years. Due to this timescale separation of at least 6 orders of magnitude, one can consider a set of fixed backgrounds, and, for each of them, evolve the dynamo models. In other words, we aim at having different snapshots, i.e. 3D dynamo solutions, each with fixed radial thermodynamical profiles corresponding to a given age of the 1D long-term evolutionary models. To schematically summarize, we employ a method that follows these steps:

1. Evolve over 10 Gyr a standard evolutionary 1D model of a contracting, non-irradiated gas giant;
2. For a given age of the evolutionary model, we implement the radially dependent thermodynamical profiles as the background state of an anelastic spherical shell MHD model, with a given choice of the dynamo numbers;
3. Evolve the 3D MHD equations in a spherical shell domain under the anelastic approximation and reach a self-sustained dynamo solution. Then we let it evolve long enough (typically up to  $\sim$ kyr of physical timescales) to average out the typical fluctuations and ensure statistical significance;
4. Repeat the process from step 2, where some of the dynamo numbers rescale (compared to the first simulation) according to the relative variation of the involved thermodynamic quantities. Note that all the dynamo numbers can be rescaled in this way, so we need further assumptions on e.g. rotation rate and viscosity, as discussed below.

<sup>1</sup> <https://github.com/magic-sph/magic>

The process can then be repeated for another planetary model or a different choice of the reference values of the dynamo numbers. In this approach, the trend of the dynamo numbers in the simulation sequence will then include the cooling information.

## 2.1. Internal structure

### 2.1.1. Long-term evolution

To model the evolutionary change of radially dependent thermodynamic quantities of gas giants, we use the public code MESA<sup>2</sup> (Paxton et al. 2011, 2013, 2015, 2018, 2019). It is a one-dimensional code that solves the time-dependent stellar structure equations and is capable of evolving low bodies including brown dwarfs and gas giants, (see Paxton et al. 2013). The equations solved are the conservation of mass, hydrostatic equilibrium, energy conservation, and the energy transport equation, respectively:

$$\frac{dm}{dr} = 4\pi r^2 \rho, \quad (1)$$

$$\frac{dP}{dm} = -\frac{Gm}{4\pi r^4}, \quad (2)$$

$$\frac{dL}{dm} = -T \frac{ds}{dt}, \quad (3)$$

$$\frac{dT}{dm} = -\frac{GmT}{4\pi r^4 P} \nabla, \quad (4)$$

where  $m$  is the mass enclosed within a radius  $r$ ,  $\rho$  is the density,  $P$  is the pressure,  $G$  the gravitational constant,  $s$  the specific entropy,  $T$  the temperature,  $L$  the internal luminosity, and  $\nabla \equiv d \ln T / d \ln P$  is the logarithmic temperature gradient, which is set to the smallest between the adiabatic gradient and the radiative gradient. In the energy equation 3, the only source term we consider is the gravitational contraction. We neglect additional sources like stellar irradiation (Guillot et al. 1996) or internal heat deposition (Komacek & Youdin 2017; Thorngren & Fortney 2018) coming from tidal (Bodenheimer et al. 2001) or Ohmic dissipation (e.g., Batygin & Stevenson 2010; Perna et al. 2010), or chemical processes like hydrogen dissociation and recombination (Tan & Komacek 2019). Such extra terms are fundamental for Hot Jupiters (see Fortney et al. 2021 for a review), but negligible for cold, weakly irradiated planets. The set of equations is closed using the MESA equation of state (Paxton et al. 2019), which, for the gas giant ranges of interest, is substantially the interpolation of the Saumon-Chabrier-van Horn equation of state for H-He mixtures (Saumon et al. 1995).

Note that these 1D evolutionary models employed do not incorporate either hydrogen-helium de-mixing layers, i.e. possible stratified layers in the convection interior, of the type mentioned in Sec. 1, or diluted cores. For all our models, we assume an interior, inert rocky core of  $10 M_{\oplus}$ , with a homogeneous density  $\rho_c = 10 \text{ g cm}^{-3}$ , and a fixed solar composition for the envelope. To illustrate the evolutionary changes, we show in Fig. 1 the different profiles for two different planets, with masses 1 and  $4 M_J$ , at ages 0.5, 1, and 10 Gyr. For comparison, we also show the profiles from the widely employed results of French et al. (2012) for the Jupiter interior. As seen in (Paxton et al. 2013), during the evolution of the planet we obtain a slow shrinking of the radius which after a few Myr of evolution is independent of the chosen initial planetary radius. The planet

slowly shrinks, the reason for which, at early ages, the total radius of the  $1 M_J$  model is larger than the current Jovian one. The internal structure is always characterized by a very thin radiative layer with a thick, fully convective isentropic shell, which encloses the inert core. The higher planetary mass ( $4 M_J$ ) shows a larger radius, gravity and temperature, and lower thermal expansion coefficients. However, the trends of the profile with age are similar to the  $1 M_J$  case. Note also that all models exhibit a non-trivial oscillating behavior of  $\Gamma$ .

### 2.1.2. Background state implementation

To run an anelastic MHD model one needs a series of thermodynamical quantities to be expressed as a function of radius. We implement MESA  $\rho(r)$ ,  $T(r)$ ,  $g(r)$ , thermal expansion coefficient  $\alpha(r)$  and the Grüneisen parameter  $\Gamma(r)$ , all shown in Fig. 1, into a 3D model. We have obtained  $\alpha$  and  $\Gamma$  in terms of readily available MESA thermodynamic profiles:

$$\Gamma = \left( \frac{\partial \ln T}{\partial \ln \rho} \right)_s - 1 \equiv \Gamma_3 - 1, \quad \alpha = -\frac{1}{\rho} \left( \frac{\partial \rho}{\partial T} \right)_p = -\frac{\chi_T}{T \chi_\rho}, \quad (5)$$

where

$$\chi_\rho \equiv \left( \frac{\partial \ln P}{\partial \ln \rho} \right)_T, \quad \chi_T \equiv \left( \frac{\partial \ln P}{\partial \ln T} \right)_\rho.$$

Transport coefficients, which we discuss and prescribe below, are the other possible thermodynamical quantities that can show a radial dependence.

To define the radial domain for the 3D models, we cut the MESA profiles both at the inner and outer radial domain. The hydrostatic background is mostly isentropic, due to the efficient convection. Close to the solid inert core, the profiles show a decrease in entropy, which is due to the simplified boundary conditions. Since a more realistic modeling of a possibly diluted core is beyond the purpose of this study, for each model we consider as the inner boundary of the shell the region where the profile is isentropic, cutting out case by case the innermost  $\sim 2\text{-}3\%$  (in radius) of the shell.

Profiles usually span more than 6 orders of magnitude (the typical outermost layer in MESA is at a fraction of a bar), with the largest drop in the 1% outermost part of the planet, where no dynamo is expected. Spherical shell dynamo models cannot handle too large density contrasts. Therefore, as is common in other anelastic dynamo models, we cut the external layers reducing the density ratio between the internal and external radius. We make sure that we always keep the hydrogen metallization pressure ( $1 \text{ Mbar}$ ) inside the domain. The maximum ratio we consider is  $\rho_{\text{ratio}} = \rho_i / \rho_o \sim 100$ , with most of our models having  $\rho_{\text{ratio}} \sim 20$ . The profiles shown in Fig. 1 have  $\rho_{\text{ratio}} \sim 20$ , and the thin endings representing an extension up to  $\rho_{\text{ratio}} \sim 100$ . Throughout this work, we use the subindex notation  $o$  ( $i$ ) for the value at the outer (inner) shell. These cuts define  $r_o$ ,  $\rho_o$ ,  $T_o$ , and  $P_o$  as well as their inner values, which can be seen in Table 1. The thin radiative outer layer usually ends at about  $\sim 1 \text{ bar}$ , which is well above the external cut. Finally, all profiles except for  $\Gamma(r)$ , are normalized to make the outer values equal to unity. This is a usual practice for many 3D hydrodynamic codes as the fundamental units are not the physical ones. MagIC, for example, works with units of the shell thickness as length scale and viscous

<sup>2</sup> <https://github.com/MESAHub/mesa>

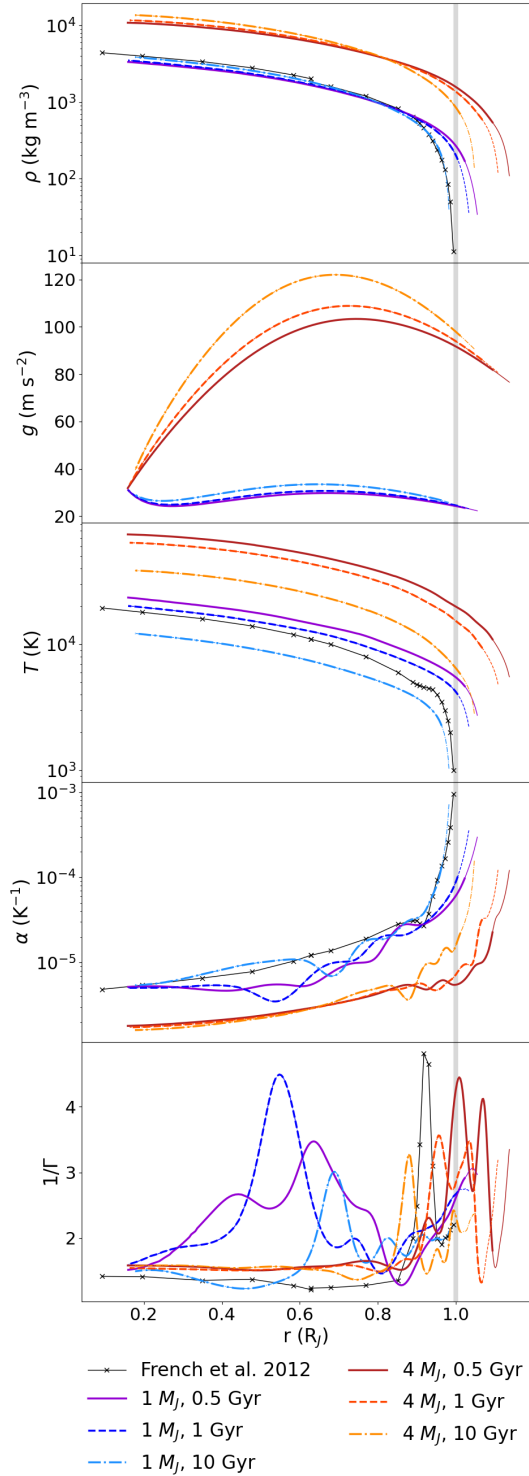


Fig. 1: MESA hydrostatic profiles of 1 and 4  $M_J$  at different evolutionary times, cut at an outer density  $\sim 100$  times (thin lines) or  $\sim 20$  times smaller than the innermost radius of the isentropic shell, just outside the core-envelope boundary. The gray lines show the Jovian values according to the popular French et al. (2012) model, and the vertical gray band reflects the current Jovian radius, as a reference. From top to bottom: density  $\rho(r)$ , temperature  $T(r)$ , gravity  $g(r)$ , thermal expansion coefficient  $\alpha(r)$ , and the inverse of the Grüneisen parameter  $\Gamma(r)$ .

timescales for units of time, see section 2.2 for the exact details.

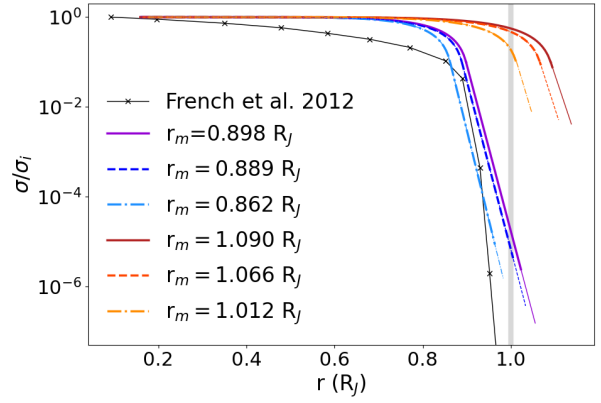


Fig. 2: Electrical conductivities normalized to their inner values ( $\sigma/\sigma_i$ ) obtained from eq. (7) for the same models shown in Fig. 1. The values of  $r_m$  in the legend correspond to the start of the exponential decay. Note that the French et al. (2012) profile has also been normalized.

Once the profiles have been cut and normalized to the inner or outer boundary (as required by the code implementation, see below), we use high-degree polynomials to generally fit any shape the profiles can take. For  $\rho(r)$ ,  $T(r)$ , and  $g(r)$  we employ a 20-degree Taylor series, which was enough to smoothly fit all cases tested here. But  $\alpha(r)$  and  $\Gamma(r)$  have some peaks and valleys that complicate the fitting procedure. With polynomials with degrees below  $\sim 100$ - $120$ , we found that the wiggles were poorly fitted. To be safe we adopted a 150-degree polynomial for both:

$$\begin{aligned} (\rho(r), T(r), g(r)) &= \sum_{n=0}^{20} (\rho_n, T_n, g_n) r^n, \\ (\alpha(r), \Gamma(r)) &= \sum_{n=0}^{150} (\alpha_n, \Gamma_n) r^n, \end{aligned} \quad (6)$$

where  $r$  ranges from  $r_i$  to  $r_o$ . Changing the reference point of the expansion did not improve quantitatively the fits (we also tried with powers of  $(r - r_o)$ ,  $(r - r_i)$  and  $(r - r_o/2)$ ). Therefore, for simplicity, we opted for powers of  $r$ , i.e. a MacLaurin series.

Unlike the fit model used by Jones (2014), the background profiles taken from MESA are almost but not exactly isentropic. To quantify this deviation we looked at the quantity  $|ds/dr| \cdot r/s$ , which usually takes values of  $10^{-4} - 10^{-5}$  with maximums near the outer cut regions of  $10^{-3}$ . This might lead to a slight energy imbalance resulting from the radial background profile itself. To ensure that this does not influence the overall dynamics, we analyze the energy balances, that is we compare the buoyancy power with viscous and Ohmic dissipation (see Sec 2.2.3 for more details).

### 2.1.3. Transport coefficients

The profiles of transport coefficients do not come directly from MESA. Although some important ingredients have evolved, like particle density, realistic profiles for diffusivities require proper *ab initio* calculations. In particular, the electrical and thermal conductivities have to take into account the degenerate state of the electron population. The pressure ionization (rather than thermal) is non-negligible

in the dense, but relatively cold (compared to stars) convective interior. Moreover, the dynamo region arguably corresponds to the transition to the metallic phase for hydrogen. In this sense, French et al. (2012) calculated the electric conductivity  $\sigma$  for a set of  $(T, \rho)$  pairs, along the modeled Jupiter adiabat. Further models about transport coefficients in pure H-He mixtures have been developed (usually neglecting the contribution of thermally ionized Alkali metals, which becomes relevant where hydrogen is molecular, Kumar et al. 2021), with relative differences in the values of  $\sigma$  by factors of a few (see Bonitz et al. 2024 for a recent review). In any case, the trend is that there is a continuous and steep increase of the conductivity for increasing pressure up to around 1 Mbar, after which the dependence with both temperature and pressure (or density) is much milder.

In order to capture these fundamental properties, we adopt the electrical conductivity profile first defined in Gómez-Pérez et al. (2010), which consists of an approximately constant conductivity in the innermost hydrogen metallic region, with a polynomial plus exponential decay towards the outer molecular region:

$$\frac{1}{\tilde{\lambda}(r)} = \tilde{\sigma}(r) = \begin{cases} 1 + (\sigma_m - 1) \left( \frac{r - r_i}{r_m - r_i} \right)^{-a} & r < r_m, \\ \sigma_m e^{-a \left( \frac{r - r_m}{r_m - r_i} \right)^{\frac{\sigma_m - 1}{\sigma_m}}} & r \geq r_m, \end{cases} \quad (7)$$

where  $\tilde{\sigma}$  and  $\tilde{\lambda}$  are the normalized conductivity and magnetic diffusivity, respectively. Note that the actual physical relation,  $\lambda = (\mu_0 \sigma)^{-1}$ , with  $\mu_0$  being the vacuum magnetic permeability, is simplified when the quantities are normalized to their innermost values:  $\tilde{\sigma} = \sigma/\sigma(r_i)$  and  $\tilde{\lambda} = \lambda/\lambda(r_i)$ . This expression ensures that both  $\tilde{\lambda}$  and  $d\tilde{\lambda}/dr$  are continuous at  $r_m$ , and qualitatively reproduce the main features. Moreover, it allows us to compare results with several previous works that have employed this profile for gas giant convection and dynamo modeling (Duarte et al. 2013, 2018; Wicht et al. 2019b,a; Gastine & Wicht 2021). They use values of  $\sigma_m$  and  $a$  ranging approximately from 0.9 to 0.01 and from 1 to 25, respectively. In our models, we have fixed  $\sigma_m = 0.1$  and  $a = 7$ , while  $r_m$  has been chosen as the radius where each MESA planetary profile reaches 1 Mbar, i.e. the pressure approximately above which hydrogen is believed to undergo metallization. The profiles of  $\tilde{\sigma}$  can be seen in Fig. 2 for the same representative models in Fig. 1.

On the other hand, for simplicity, in this study, we keep both the kinematic viscosity  $\nu$  and thermal diffusivity  $\kappa$  constant within the same model. In section 3.6, we will come back to the impact and caveats of this choice and the related assumption about the Prandtl numbers (section 2.2.4).

## 2.2. 3D numerical dynamo model

The next step is the fundamental one: we perform 3D MHD spherical shell simulations using the public code MagIC with the anelastic approximation (Gastine & Wicht 2012). It is a pseudo-spectral code that uses the spherical harmonic decomposition in the angular directions, i.e.  $\theta$  and  $\phi$ , and Chebyshev polynomials in the radial direction  $r$ . MagIC has been used for both stellar and planetary models, including for Jupiter and Saturn dynamos, e.g. Duarte et al. (2018); Wicht et al. (2019b); Gastine & Wicht (2021); Yadav et al. (2022), as well as being tested in convection and dynamo benchmarks Christensen et al. (2001); Jones et al. (2011). Here the anelastic approximation is employed, which is typically used for modeling the density-stratified low-Mach

number convection flows in gas giants and stars Braginsky & Roberts (1995); Lantz & Fan (1999).

The shell is filled with a finitely conducting fluid rotating along the vertical axis  $\hat{z}$  with a constant angular velocity  $\Omega$ , and the background profiles, which we set up as explained in section 2.1.2. The geometry is set by the aspect ratio  $\eta = r_i/r_o$ . We work in dimensionless units using the shell thickness  $d = (r_o - r_i)$  as the length unit and the viscous diffusion timescale  $d^2/\nu$  as the time unit. Magnetic fields are in units of  $(\rho_o \mu_o \lambda_i \Omega)^{1/2}$ , where  $(\mu_o \lambda_i) = 1/\sigma(r_i)$  is the magnetic diffusivity at the inner boundary. Convection is set by a fixed entropy gradient  $\Delta s$ , and this difference serves as the non-dimensional units for  $s$ .

The equations solved are, respectively, the mass continuity equation, the momentum equation, the entropy equation, the induction equation, and the solenoidal condition for the magnetic field:

$$\nabla \cdot (\tilde{\rho} \mathbf{u}) = 0, \quad (8)$$

$$\frac{\partial \mathbf{u}}{\partial t} + \mathbf{u} \cdot \nabla \mathbf{u} = -\nabla \left( \frac{p'}{\tilde{\rho}} \right) - \frac{2}{E} \mathbf{e}_z \times \mathbf{u} - \frac{Ra}{Pr} \tilde{g} \tilde{\alpha} \tilde{T} s' \mathbf{e}_r + \frac{1}{Pm E \tilde{\rho}} (\nabla \times \mathbf{B}) \times \mathbf{B} + \frac{1}{\tilde{\rho}} \nabla \cdot \mathbf{S}, \quad (9)$$

$$\tilde{\rho} \tilde{T} \left( \frac{\partial s'}{\partial t} + \mathbf{u} \cdot \nabla s' \right) = \frac{1}{Pr} \nabla \cdot (\tilde{\rho} \tilde{T} \nabla s') + \frac{Pr Di}{Ra} (Q_v + Q_\lambda), \quad (10)$$

$$\frac{\partial \mathbf{B}}{\partial t} = \nabla \times (\mathbf{u} \times \mathbf{B}) - \frac{1}{Pm_i} \nabla \times (\tilde{\lambda} \nabla \times \mathbf{B}), \quad (11)$$

$$\nabla \cdot \mathbf{B} = 0, \quad (12)$$

where the traceless rate-of-strain tensor  $S_{ij}$  and the viscous and Ohmic heating terms,  $Q_v$  and  $Q_\lambda$  are defined by:

$$S_{ij} \equiv 2\tilde{\rho} \left( e_{ij} - \frac{1}{3} \delta_{ij} \nabla \cdot \mathbf{u} \right), \quad e_{ij} \equiv \frac{1}{2} \left( \frac{\partial u_i}{\partial x_j} + \frac{\partial u_j}{\partial x_i} \right), \\ Q_v \equiv 2\tilde{\rho} \left( e_{ij} e_{ij} - \frac{1}{3} (\nabla \cdot \mathbf{u})^2 \right), \quad Q_\lambda \equiv \frac{\tilde{\lambda}}{Pm^2 E} (\nabla \times \mathbf{B})^2.$$

The dimensionless Ekman, Rayleigh, Prandtl, and magnetic Prandtl numbers are respectively defined as:

$$E \equiv \frac{\nu}{\Omega d^2}, \quad Ra \equiv \frac{\alpha_o g_o T_o d^3 \Delta s}{c_p \nu \kappa}, \quad Pr \equiv \frac{\nu}{\kappa}, \quad Pm \equiv \frac{\nu}{\lambda_i}.$$

All the quantities marked with a tilde (Sec. 2.1.2 and 2.1.3) are static in time, radially dependent, and normalized to their outer values except  $\lambda$ , which due to its decaying nature on the outer radial regions it is normalized to its innermost value.

### 2.2.1. Boundary conditions

We assume stress-free and impenetrable boundary conditions for the velocity at both inner and outer radii,  $r = r_i, r_o$ :

$$u_r = \frac{\partial}{\partial r} \left( \frac{u_\theta}{r} \right) = \frac{\partial}{\partial r} \left( \frac{u_\phi}{r} \right) = 0.$$

We employ constant entropy at both boundary conditions:

$$s'(r = r_o) = 0, \quad s'(r = r_i) = 1.$$

The material outside the outer radius is electrically insulating, i.e. the magnetic field matches a potential field. At the inner boundaries, we impose a perfectly conducting core.

### 2.2.2. Numerical technique

MagIC solves the set of equations (8 - 12) with the above boundary conditions by expanding the mass-flux and the magnetic fields into poloidal and toroidal potentials:

$$\begin{aligned}\tilde{\rho}\mathbf{u} &= \nabla \times (\nabla \times W \mathbf{e}_r) + \nabla \times Z \mathbf{e}_r, \\ \mathbf{B} &= \nabla \times (\nabla \times g \mathbf{e}_r) + \nabla \times h \mathbf{e}_r.\end{aligned}$$

The quantities  $W$ ,  $Z$ ,  $g$ ,  $h$ ,  $s'$  and  $p'$  are expanded up to  $l_{max}$  in spherical harmonic degree and  $N_C$  in Chebyshev polynomials. The equations are time-stepped by advancing nonlinear and Coriolis terms using an explicit second-order Adams-Bashforth scheme and the remaining terms are time-advanced using the implicit Crank-Nicolson algorithm. For more details see Glatzmaier (1984); Christensen & Wicht (2007).

### 2.2.3. Diagnostic parameters

To characterize the numerical dynamo solutions we make use of several diagnostic quantities. Usually, we take averages in time or in space, either over the whole volume  $V$ , or over spherical surfaces, to show the radial dependency:

$$\begin{aligned}\|a\|(r, t) &= \int a(r, \theta, \phi, t) \sin\theta d\theta d\phi, \\ \langle a \rangle(t) &= \frac{1}{V} \int a(r, \theta, \phi, t) dV, \quad \bar{a} = \frac{1}{\Delta t} \int_r^{r'+\Delta t} a(t) dt.\end{aligned}$$

For the time averages, we perform them after a stationary state has been reached, and we typically monitor the dimensionless hydrodynamic and magnetic Reynolds numbers, the Rossby number, and the Elsasser number:

$$\begin{aligned}Re &= \sqrt{\langle u^2 \rangle}, \quad Rm = \frac{1}{V} \int_{r_i}^{r_o} \frac{\sqrt{\|\mathbf{u}\|^2}}{\lambda} r^2 dr, \\ Ro &= \frac{Rm E}{Pm}, \quad \Lambda = \left\langle \frac{\mathbf{B}^2}{\tilde{\rho}\lambda} \right\rangle.\end{aligned}$$

The total kinetic and magnetic energy, which are in units of  $\rho_0 d^5 E^2 \Omega^2$ , are:

$$E_{kin} = \frac{1}{2} \overline{\langle \tilde{\rho} \mathbf{u}^2 \rangle}, \quad E_{mag} = \frac{1}{2} \overline{\langle \frac{1}{EPm} \mathbf{B}^2 \rangle}.$$

We define the dipole fraction,  $f_{dip} = E_{mag, l=1} / E_{mag}$ , as the ratio of the magnetic energy stored in dipolar components (axisymmetric and non-axisymmetric), divided by the total magnetic energy.<sup>3</sup>

To study energy dissipation we use the buoyancy power:

$$P_\nu(t) \equiv \frac{RaE}{Pr} \langle \tilde{\alpha} \tilde{T} \tilde{g} s' u_r \rangle. \quad (13)$$

We use the sub-index  $\nu$  to emphasize that the quantity is calculated in viscous timescales. For comparison with other works, we also use rotation time-scale, see Sec. 3.7. For a well-resolved numerical run, once a steady-state solution has been reached, the buoyancy power must be equal to the

<sup>3</sup> Note that our definition differs from another widely used one, that is the ratio between the axisymmetric dipole component to the magnetic energy in the spherical harmonic degrees  $l \leq 12$  at  $r_o$ , and the total, e.g. Christensen & Aubert (2006).

sum of viscous and Ohmic dissipation rates, which are respectively defined as:

$$D_{visc}(t) \equiv \langle S^2 \rangle, \quad D_{ohm}(t) \equiv \frac{1}{EPm^2} \langle \tilde{\lambda} (\nabla \times \mathbf{B})^2 \rangle. \quad (14)$$

Another quantity to monitor is the fraction of energy dissipated by Joule heating alone, i.e. the Ohmic fraction  $f_{ohm} = D_{ohm} / P_\nu$ . Once a statistically steady state has been reached, the input buoyant power must balance with the viscous and Ohmic diffusion. To evaluate whether the numerical solution has good time and spatial invariance and also if the background state has much influence on the energy balance, we assess the power imbalance by its proxy  $f_P = |P_\nu - D_{visc} - D_{ohm}| / P_\nu$ .

Finally, we study the time-averaged kinetic and magnetic spectra, i.e. the distribution of the energy over different multipoles of order  $l$ , which MagIC already has implemented as a user-friendly output. We inspect the spectra for each model, in particular, to ensure that the resolution is large enough so that the maximum dissipation, that is  $l(l+1)E(l)$ , is resolved.

### 2.2.4. Parameter evolution and model descriptions

As explained in 2.1.2, once the MESA profiles have been cut close to the desired  $\rho_{ratio}$ , we extract  $\Delta T$ ,  $r_o$ ,  $r_i$  and  $r_m$ , from which we deduce  $\eta$  and  $\chi_m$ . The corresponding physical values can be recovered by knowing the units in which each quantity is expressed and the values from the MESA profile, for example, using the thickness of the physical shell thickness  $d_{phys} = r_{o,phys}(1 + \eta)$ . The real quantities of the planet, which reflect the evolutionary changes, are used to evolve the dynamo parameters. Since, as mentioned above, the real physical values  $E$  and  $Ra$  are computationally inaccessible, we can still use their dependence on the physical values that change during the long-term evolution. In particular, the shell thickness  $d = r_o - r_i$  and the temperature difference  $\Delta T$  enter in the definition of the Ekman,  $E(t) \sim d(t)^{-2}$ , and Rayleigh numbers,  $Ra(t) \sim d(t)^3 \Delta T(t)$ . Therefore, we will consider a series of ages, for which, after having found a suitable pair of  $E_0$  and  $Ra_0$ , that produce convection and dynamo for the setup with  $d_0$  and  $\Delta T_0$  corresponding to a given age, the values  $E'$  and  $Ra'$  of the rest of models in that series are setup by scaling with  $d(t)$  and  $\Delta T(t)$ :

$$E' = E_0 \frac{d_0^2}{d^2}, \quad Ra' = Ra_0 \frac{d_0^3 \Delta T'}{d^3 \Delta T_0}.$$

Note that here we make use of two assumptions: (i) the diffusivities at a given radius remain constant in time, which implies that we consider the same values of both  $Pr$  and  $Pm$  along a sequence and that the change in  $E$  only comes from the contraction of the planet; and (ii) planetary rotation is constant in time. The latter assumption is well justified if one considers the possible relevant torque acting on a gas giant. Batygin (2018) studied the evolution of rotation, considering the magnetic coupling between the planetary interior and the quasi-Keplerian motion of the disk in the planetary formation stages. This results in efficient braking of the planetary spin that stops evolving after 1 Myr with a value similar to the Jovian period, reaching a terminal rotation rate, which can hardly change later. Note that our earliest model is at 100 Myr, for which the rotation can be safely considered constant. In this sense, cold

Table 1: Parameters of the 1D models MESA models for the  $1M_J$  and  $4M_J$  at different times and density cuts, and the corresponding values of  $\eta = r_i/r_o$ ,  $\chi_m = r_m/r_o$ , the dimensionless mass of the shell  $M = 4\pi \int_{r_i}^{r_o} r^2 \frac{\rho(r)}{\rho_o} dr$ , and the dynamo parameters  $E$ ,  $Ra$  (after calibrating them in one case as described in the text).

Model	$\rho_{ratio}$	$\rho_o(\text{g}\cdot\text{cm}^{-3})$	$\Delta T$ (K)	$T_o$ (K)	$P_o$ (kbar)	$r_o(R_J)$	$\eta$	$M$	$\chi_m$	$E$	$Ra$
$1M_J$ 1 Gyr	10.0	0.351	14973	5220	240	0.967	0.165	26.48	0.919	$1.23\cdot 10^{-5}$	$7.92\cdot 10^8$
$1M_J$ 1 Gyr	39.8	0.0881	17093	3100	14.9	1.022	0.156	89.66	0.869	$1.08\cdot 10^{-5}$	$1.10\cdot 10^9$
$1M_J$ 1 Gyr	97.9	0.0358	17962	2231	3.46	1.034	0.155	214.0	0.860	$1.05\cdot 10^{-5}$	$1.20\cdot 10^9$
$1M_J$ 0.4 Gyr	19.9	0.165	19782	4858	55.6	1.030	0.164	47.36	0.874	$1.08\cdot 10^{-5}$	$1.27\cdot 10^9$
$1M_J$ 0.5 Gyr	19.6	0.171	18847	4665	57.3	1.023	0.156	45.58	0.878	$1.08\cdot 10^{-5}$	$1.22\cdot 10^9$
$1M_J$ 0.7 Gyr	19.8	0.172	17345	4306	54.8	1.014	0.166	48.03	0.881	$1.12\cdot 10^{-5}$	$1.05\cdot 10^9$
$1M_J$ 1 Gyr	19.8	0.177	16158	4002	54.5	1.005	0.159	46.91	0.884	$1.12\cdot 10^{-5}$	$9.81\cdot 10^8$
$1M_J$ 1.5 Gyr	19.6	0.181	15004	3716	54.0	0.998	0.1628	47.47	0.884	$1.15\cdot 10^{-5}$	$8.78\cdot 10^8$
$1M_J$ 2.1 Gyr	19.9	0.181	13999	3428	51.0	0.992	0.169	49.61	0.887	$1.18\cdot 10^{-5}$	$7.87\cdot 10^8$
$1M_J$ 2.8 Gyr	19.9	0.184	13278	3220	50.0	0.987	0.170	49.77	0.890	$1.20\cdot 10^{-5}$	$7.33\cdot 10^8$
$1M_J$ 3.5 Gyr	19.9	0.187	12424	2983	49.2	0.981	0.171	50.07	0.889	$1.21\cdot 10^{-5}$	$6.71\cdot 10^8$
$1M_J$ 5 Gyr	19.9	0.190	11742	2779	48.3	0.975	0.172	52.29	0.892	$1.23\cdot 10^{-5}$	$6.22\cdot 10^8$
$1M_J$ 6.5 Gyr	19.7	0.192	11031	2591	47.3	0.970	0.183	53.35	0.892	$1.28\cdot 10^{-5}$	$5.52\cdot 10^8$
$1M_J$ 10 Gyr	20	0.193	10180	2327	44.7	0.964	0.184	53.35	0.894	$1.30\cdot 10^{-5}$	$4.98\cdot 10^8$
$4M_J$ 0.5 Gyr	99.8	0.109	69086	5533	33.6	1.137	0.140	32.20	0.959	$8.37\cdot 10^{-6}$	$6.50\cdot 10^9$
$4M_J$ 1 Gyr	97.9	0.120	59273	4829	33.9	1.109	0.148	31.26	0.961	$8.98\cdot 10^{-5}$	$5.02\cdot 10^9$
$4M_J$ 10 Gyr	99.5	0.137	36481	2880	27.7	1.048	0.169	31.81	0.967	$1.06\cdot 10^{-5}$	$2.42\cdot 10^9$
$0.3M_J$ 5 Gyr	3.00	0.545	3022	3754	563	0.650	0.275	16.89	0.879	$3.61\cdot 10^{-5}$	$3.18\cdot 10^7$
$0.7M_J$ 5 Gyr	19.6	0.144	8927	2243	25.1	0.944	0.190	53.69	0.843	$1.37\cdot 10^{-5}$	$4.01\cdot 10^8$
$2M_J$ 5 Gyr	19.7	0.338	20486	4195	198	1.015	0.167	50.13	0.955	$1.12\cdot 10^{-5}$	$1.24\cdot 10^9$
$4M_J$ 5 Gyr	19.7	0.671	38765	6762	1060	1.025	0.159	47.94	1.000	$1.08\cdot 10^{-5}$	$2.49\cdot 10^9$

giants are expected to be fast rotators ( $Ro < 0.12$ ), possibly hosting planetary dynamos similar to the ones found in dipole-dominated numerical solutions with very low  $E$  (Davidson 2013; Yadav et al. 2016; Schwaiger et al. 2019). In this scenario there is a quasi-geostrophic balance (Coriolis and pressure forces) at the largest scales, followed by an ageostrophic magneto-Archimedean-Coriolis balance (Coriolis, buoyancy and Lorentz forces).

With these assumptions, we consider five sets of dynamo models: (i) a long series with a total of 12 evolutionary stages, ranging from 0.1 to 10 Gyr for a  $1M_J$  planet; (ii) different density ratios for the same  $1M_J$  model at 1 Gyr; (iii) different planetary mass with  $\rho_{ratio} \approx 20$ ; (iv) several models with  $Pm$  and  $Pr$  different from 1; and (v) a  $4M_J$  mass series with  $\rho_{ratio} \approx 100$ . Note that, when a different mass is chosen, the radial profiles change (see Fig. 2), so that, using eq. (7) with the above-mentioned values of the free parameters  $a$  and  $\tilde{\sigma}_m$ , we have to adapt the density contrast  $\rho_{ratio}$  to include the drop of conductivity in the outer layers of our shell, without, at the same time, having too low values of  $\sigma$ . For this reason, the series of  $4M_J$  has a higher  $\rho_{ratio}$  (the exponential drop of  $\sigma$  would have been cut out with  $\rho_{ratio} \approx 20$ ). For the same reason, the  $0.3M_J$  model has a lower contrast,  $\rho_{ratio} \sim 3$ . The alternative would have been to consider an equally arbitrary change of the free parameters in eq. (7). how our parameter exploration allows us to assess the impact of  $\rho_{ratio}$  and other parameters on the results. In Table 1, we show the input values for the 3D simulations, together with the parameters of the background profiles, coming from MESA 1D long-term evolution.

### 3. Results

#### 3.1. Preliminary exploration of parameters

Our first goal is to look at how the dynamo solutions depend on mass and age for a given evolutionary sequence of background thermodynamic setups (Table 1). Therefore, the first requirement is to move in a range of parameters for which both convection and dynamo are operating for all models. This practically means that we need to find a feasible range of  $Ra$  and  $E$  (which, within a sequence of models, have rel-

ative variations set by  $\Delta T$ ,  $T_o$  and  $d$ , Table 1), for which convection and dynamo action are present in the entire sequence, keeping in mind that the chosen values are orders of magnitude away from the realistic values, as mentioned above. To find such feasible ranges, we need to perform a preliminary exploration of parameters. At the same time, we assess the sensitivity of results on other parameters. We summarize in this sub-section the four main steps we have taken for this overall assessment.

First, in order to locate the region with viable dynamo solutions, we performed low- and medium-resolution runs for one specific model, the  $1M_J$  10 Gyr. It is the oldest and coldest one of the  $1M_J$  sequence, i.e. with the lowest value of  $\Delta T$ , implying also the lowest value  $Ra$  among the series, i.e., the less favorable to convection. We spanned the ranges  $10^{-5} < E < 10^{-3}$ ,  $10^6 < Ra < 10^{10}$  with  $Pm=Pr=1$  and a relatively low resolution,  $(N_r, N_\theta, N_\phi) = (193, 192, 384)$ . For  $E \leq 10^{-4}$  we obtained convection for  $Ra \gtrsim 10^7$ , and, additionally, magnetic field growth for  $Ra \gtrsim 5\cdot 10^7$ .

Second, for the  $1M_J$  10 Gyr case with  $E=10^{-5}$ ,  $Ra=5\cdot 10^8$  (the reference model in the rest of this subsection), we explore the Prandtl numbers in a relatively easily accessible range  $0.25 < Pm, Pr < 4$ . This was done to discuss the impact of our assumptions of constant-in-time diffusivities (Sec. 2.1.3). The results of this exploration are shown in Sec. 3.6, for high-resolution models, as well as different evolutionary ages.

Third, for the same reference model ( $E=10^{-5}$ ,  $Ra=5\cdot 10^8$ ,  $Pm=Pr=1$ ), we explored the sensitivity on the parameters  $a$  and  $\sigma_m$  that define the slope of  $\tilde{\lambda}(r)$  in the outermost layers. For a wide range of values (i.e.,  $0.07 < \sigma_m < 0.9$ ,  $5 < a < 15$ ) we indeed recover the results of Duarte et al. (2013), that is the strong equatorial jet remains confined to the weaker conducting outer region and does not interfere with the deeper dynamo action. As previously mentioned, we finally opted for rather low values for both  $\sigma_m$  of 0.1 and  $a$  of 7. These values are similar to the ones used by Gastine & Wicht (2021), whose model approximately reproduces the French et al. (2012) profiles. For numerical stability reasons, we did not use higher values of  $a$ , i.e. steeper exponential drops, because the hydrogen metallic region of some of our models is already quite

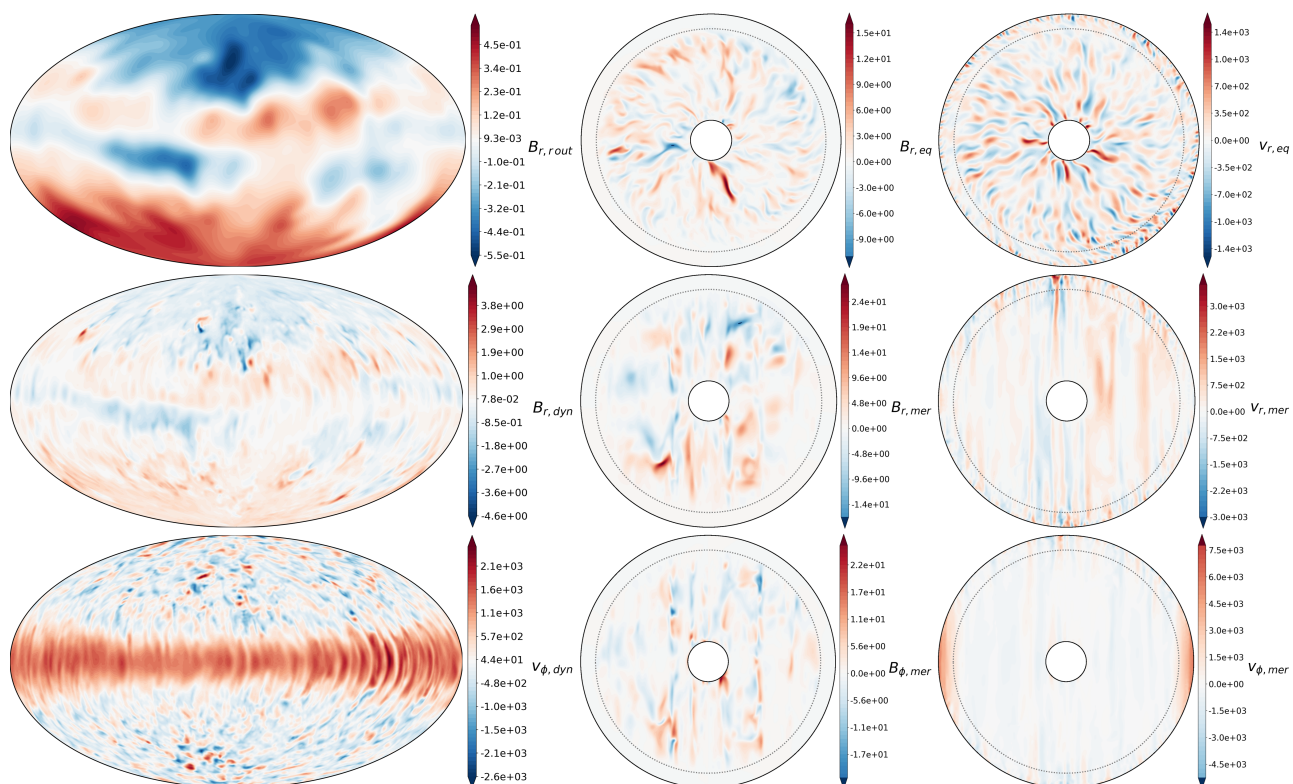


Fig. 3: Snapshots of the saturated solution for the representative  $1 M_J$  1 Gyr model. *Left column*: maps of  $B_r$  at the outermost layer of our domain,  $B_r$  at  $r = r_m$ ,  $v_\phi$  at  $r = r_m$ , from top to bottom. *Center*: equatorial slice of  $B_r$ , meridional slice of  $B_r$ , meridional slice of  $B_\phi$ . *Right*: equatorial slice of  $v_r$ , meridional slice of  $v_r$ , meridional slice of  $v_\phi$ . In the central and right panels, the location of  $r_m$  is marked with dotted gray lines in both equatorial and meridional cuts. The color bars indicate the values in code units.

deep ( $\chi_m > 0.85$ ) leading to too high values of  $\tilde{\lambda}(r)$  near the outer surface. Similarly, we studied the effect of  $\rho_{ratio}$  on several diagnostic quantities, see App. A for more details. Given the non-negligible effects of choosing different values of  $\rho_{ratio}$ , below we will compare models with the same  $\rho_{ratio}$ , to avoid additional biases.

Fourth, again for the same reference model, we tested different boundary conditions. Integrated quantities such as  $Rm$  or  $E_{kin}$  as well as convection patterns did not change appreciably if rigid boundary conditions were applied at the inner core. The radial distributions showed a drop in velocity in a very thin region ( $< 1\%$ ) of the radius. For the magnetic field, we tested for perfect conductor and insulating for the inner core and insulating, perfect conductor, and pseudo-vacuum at the outer radii. We found no relevant differences in the internal dynamo.

Considering the explored values of  $Ra$  and  $E$  for these low-resolution test, we set  $Ra = 1.3 \cdot 10^{-5}$  and  $E \approx 5 \cdot 10^8$  for the  $1 M_J$  10 Gyr model with a  $\rho_{ratio} \approx 20$ . This choice allows for the rescaled values for the rest of the sequence to be in a range that allows dynamo action. Using the definition of  $E$ ,  $Ra$ , we scaled their values in each run with the corresponding values of  $T$ ,  $\Delta T$ ,  $d$ , as described in Sec. 2.2.4. Most models use a resolution of  $(N_r, N_\theta, N_\phi) = (288, 256, 512)$ . As an exception, the  $4 M_J$   $\rho_{ratio} \approx 100$  runs use a grid of  $(385, 320, 340)$ .

Finally, we employed a strategy to save computational time, inspired by other spherical shell dynamo works (Christensen & Aubert 2006). The idea is that the final solution does not depend on whether the initial conditions are taken from another saturated dynamo model or whether they are the usual  $\mathbf{u} = 0$  with a small perturbation of both  $\mathbf{B}$

and  $T'/s'$ . This particularly suits our case, since the relative changes of dynamo parameters from one set-up to another are not large, and the solution of the new setup is reached much faster than starting from a  $\mathbf{u} = 0$  state. In App. B we show the results of some specific numerical experiments that support this strategy.

We now proceed to the main results. We refer to App. D for a table with detailed values of the time-averaged output dynamo numbers and the other quantities used as diagnostics.

### 3.2. Dynamo solutions: general behavior

In Fig. 3 we show snapshots (maps and slices of some velocity and magnetic field components) of the  $1 M_J$  1 Gyr saturated dynamo solution, a representative case. The other models we obtain are qualitatively similar among themselves, in terms of morphology of velocity and magnetic fields. The biggest differences are the relative average strengths of  $\mathbf{u}$  and  $\mathbf{B}$  and the magnetic field dipolarity, which we discuss below. All the models have a strong equatorial flow that goes deep, down to the dynamo region. Both velocity and magnetic fields show a westward drift in the inner parts. The magnetic field is mostly constrained under  $r < r_m$ , where convection is also stronger, as seen in  $u_r$ . As expected from rotation-dominated convection, columnar structures in the direction of the rotation axis (Zhang & Busse 1987; Ardes et al. 1997; Simev & Busse 2003), as shown in the meridional slices. Generally speaking, our numerical solutions are similar to the ones reported by other



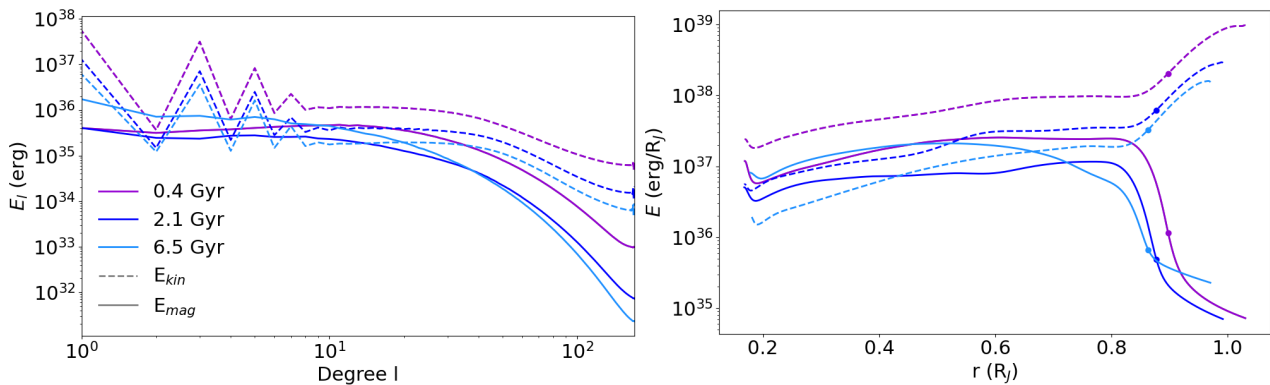


Fig. 4: Magnetic (solid) and kinetic (dashes) energy distribution over the multipole degrees  $l$  (left), and over the radius (right), for three models representing the same  $1 M_J$  planet at different evolutionary stages (0.4, 2.1 and 6.5 Gyr). Spectra have been averaged in time over the saturated state. The location of  $r_m$  is marked with a dot in the radial plots. The physical units are obtained by multiplying by the factor  $\rho_0 d^5 E^2 \Omega^2$ , where  $\rho_0$ ,  $d$  and  $E$  depend on each model and  $\Omega = 1.76 \cdot 10^{-4}$ , that is the Jovian value.

works for Jovian-like dynamos having non-constant electrical conductivity (Jones 2014; Duarte et al. 2018).<sup>4</sup>

The dynamo solutions we find are generally less dipole-dominated than their incompressible (Boussinesq), counterparts with similar dynamo parameters (i.e.  $Ra$ ,  $E$ ,  $Pr$ , and  $Pm$ ). However, we note that we did not explore values for  $Pr$  lower than 0.1 with  $Pm > 1$ , where dipole-dominated solutions have been found (Jones 2014; Tsang & Jones 2020). We restrict ourselves to a less demanding parameter space with a bigger liberty of parameter exploration but with the caveat of possibly obtaining less dipole-dominated models. Also, similarly to Yadav et al. (2013), for all runs shown here we obtain  $Nu > 2$  at both top and bottom surfaces, ensuring a fully developed convection. The Nusselt number  $Nu$  is the ratio of the total transported heat flux to the conducted heat flux.

Note also that, for gas giants, the definition of dynamo surface is not absolute. As hydrogen gradually transitions outward from metallic to molecular, the electrical conductivity and electrical currents are quickly (but not abruptly) damped over a finite region. For our models, the most obvious choice for the dynamo surface is the radius where the exponential decay for  $\sigma$  starts, that is  $r_m$ . To obtain a more physically justified definition for the dynamo surface, we follow Tsang & Jones (2020) by computing the magnetic energy spectra at different radii,  $F_l(r)$ . They define the dynamo surface,  $r_{dyn}$ , as the radius within which the slope of the Lowes' spectrum (i.e., a potential solution extrapolated back from the outermost layer to the interior) diverges from the slope of the simulated  $F_l(r)$ . A similar analysis for some of our models is shown in App. C, finds that this definition of dynamo surface always gives values very close to  $r_m$ .

### 3.3. Evolutionary changes

We now focus on how the solutions vary along the longest sequence of models, the  $1 M_J$  planet with  $\rho_{ratio} = 20$  and  $Pm = Pr = 1$ . The shell-averaged spectral distribution and radial distribution of magnetic (solid lines) and kinetic (dashed lines) energy are shown in Fig. 4. We focus on three representative ages: 0.4, 2.1, and 6.5 Gyr.

In the left panel, kinetic spectra show a drop of about 1.5 orders of magnitude or more from the integral to viscous

scales, while the magnetic spectra decrease by at least 3 orders. The tooth saw shape on the lowest multipole side are associated to the external jet that we see in all of our runs. This behavior is not seen for the  $m$  spectrum, as purely longitudinal structures are canceled during spherical harmonic integration sharing the same  $m$ .

For higher multipoles, the spectrum plateaus before reaching the viscous scale and dropping off. Comparing the three different models, the overall shape of the kinetic spectra do not significantly change other than a constant decrease in time throughout all harmonic degrees. The magnetic spectra show a similar diffusive scale, which is approximately located at the same  $l$  as the viscous diffusive scale (compatible with  $Pr = Pm = 1$ ), although the knee is less pronounced. With the usual measure of dipolarity, it ranges  $0.3 > \int_{dip, l < 12}^{axi, surf} = E_{mag}(r_0)_{l=1, m=0} / E_{mag}(r_0)_{l \leq 12} > 0.8$ . Depending on the work, this could be considered multipolar or dipolar (Christensen & Aubert 2006; Yadav et al. 2013; Zaire et al. 2022). Magnetic spectra show a clear evolution with age: the relative weights of high multipoles tend to decrease, while the strength of the large scales slightly increases. This inversion leads to an increase in the total dipolarity (see discussion below).

From the radial energy distributions, shown in the right panel of Fig. 4, we can observe that  $E_{kin}(r)$  increases almost monotonically outward, but the steepest changes are for the outermost layers,  $r \gtrsim r_m$ , due to the appearance of the equatorial zonal wind, where there is less density and less magnetic drag than in the interior. Similarly to the spectra, the kinetic radial distribution does not show a clear variation with age. The radial profile  $E_{mag}(r)$  and its change with age shown by is instead more complex. The radial profile peaks at radii slightly smaller than  $r_m$ , after which it significantly drops, following the  $\sigma(r)$  profiles (Fig. 2). Comparing different evolutionary ages, the innermost region of the radial distribution does not show a clear trend, with a slight increase in the deepest regions for late-age models. On the other hand, the layers  $\sim 10$ -20 % below  $r_m$  show a steady decrease with age, see Sec. 3.5.

The overall changes between runs are gradual and we find that few models can already asses the general behavior. Several time and volume-averaged diagnostic quantities are shown as a function of evolutionary models in Fig. 5. As expected during a gas giant planetary cool-down,  $Rm$  decays approximately like a power law in time.  $Ro$  and  $P$

<sup>4</sup> They use a different code with a strictly isentropic background profile that fits  $T(r)$ ,  $\rho(r)$  and  $\sigma(r)$  from French et al. (2012).

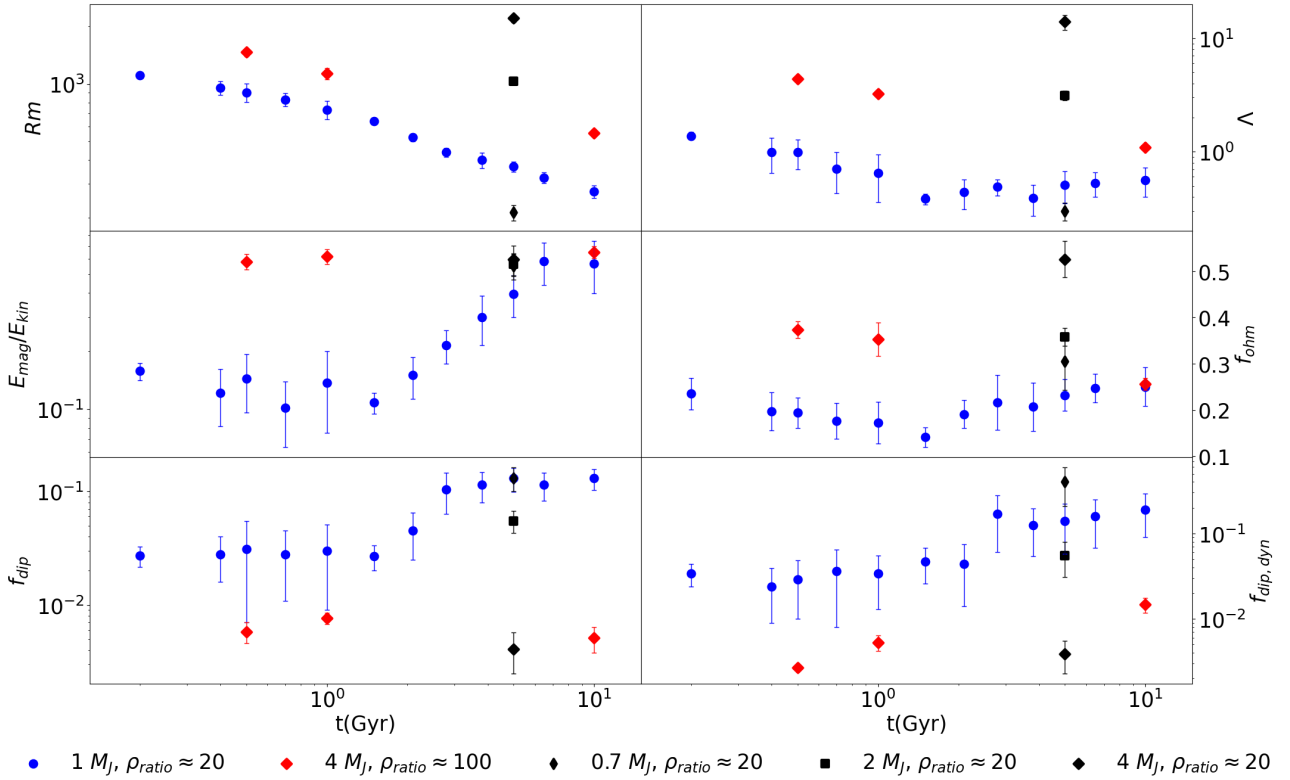


Fig. 5: Diagnostics as a function of the age for different masses, all with  $Pm = Pr = 1$ . From left to right and top to bottom, the magnetic Reynolds number, the Elsasser number, the magnetic to kinetic energy ratio, the Ohmic fraction, total dipolarity, and dipolarity at the dynamo surface. Note that the  $4 M_J$  runs at 0.5, 1, and 10 Gyr have a higher  $\rho_{ratio}$  (see text).

also behave similarly, thus they are not shown to avoid repetition. All of these quantities are dependent on  $u_{rms}$  or at least one of its components. This reflects the fact that the mean velocity is dictated by the buoyancy input parameter  $Ra$ , which is proportional to the temperature difference in the convective shell. In Fig. 5 we can also see that the dipolarity  $f_{dip}$  seems to not significantly change in time, except from a mild increase between the 1.5 and 3.8 Gyr. This led us to think that we are having a transition between a multipolar or weakly dipolar-dominated regime to a strong dipolar-dominated regime. This increasing trend is not very clear with  $f_{dip,l<12}^{axi,surf}$  (for the  $1 M_J$  series, they take values from 0.3 to 0.8). As an alternative, we obtained the average  $f_{dip}$  over the volume 5% near the dynamo surface,  $f_{dip,dyn}$ . As seen in Fig. 5,  $f_{dip,dyn}$  shows a gradual growth with a similar jump seen in  $f_{dip}$ .

This transition from multipolar to dipolar dynamo was observed also by Zaire et al. (2022) for dynamos in stratified stellar interiors, modeled with shallower shells ( $r_i/r_o = 0.6$ ) and different  $\rho_{ratio}$  and  $Ra$ . They obtained a threshold  $F_I/F_L$  (i.e. the relative importance of inertial over Lorentz forces) below which multipolar dynamos collapse into dipolar dynamos. They also reported that  $E_{kin}/E_{mag}$  can equally well capture this magnetic morphology transition and found this transition at about  $E_{kin}/E_{mag}=0.7$ . In Fig. 6 we show both  $f_{dip,l<12}^{axi,surf}$  and  $f_{dip,dyn}$  as a function of  $E_{kin}/E_{mag}$  for the  $1 M_J, Pr = Pm = 1$  series. We also report two distinctive populated areas, low dipolarity with high  $E_{kin}/E_{mag}$  and high dipolarity with lower  $E_{kin}/E_{mag}$ . This abrupt change of magnetic field morphology seems to be better reflected with  $f_{dip,dyn}$ . A good definition for a dipole-dominated dynamo could be  $f_{dip,dyn} > 0.1$ , which is

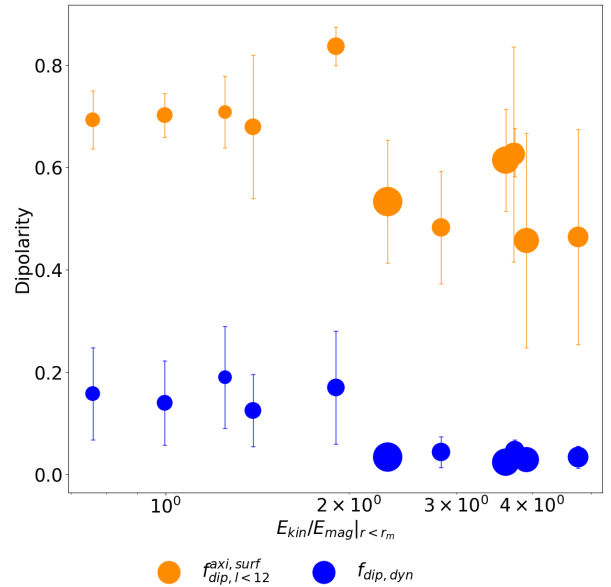


Fig. 6: Dipolarity measurements as a function of the inverse of equipartition for the  $1 M_J, Pr = Pm = 1$  models.

possibly compatible with Yadav et al. (2013) or Zaire et al. (2022) definitions:  $f_{dip,l<12}^{axi,surf} > 0.3, 0.5$ , respectively. These dipole-related quantities are usually the most fluctuating integrated quantities in saturated dynamo solutions, as they are very sensitive to the specific magnetic field configuration.

In any case, our largest evolutionary trend shows a transition from a multipolar to a dipolar regime in the middle of our series. Within the more multipolar part of the series,  $\Lambda$  and  $f_{ohm}$  decay in time, and  $E_{mag}/E_{kin}$  also seem to decrease, but in a more subtle way. In the dipolar regime, these trends reverse:  $\Lambda$  and  $f_{ohm}$  plateau and show a slight increase; the ratio  $E_{mag}/E_{kin}$  grows noticeably. Following Jupiter and Saturn’s magnetic fields (Connerney et al. 2022; Cao et al. 2023), gas giant dynamos are expected to live in a parameter space region with dipole-dominated solutions, thus the expected evolution would be of the latter part of our series. Moreover, the Jovian value for  $Pm$  is expected to be  $\sim 10^{-6}$ , meaning that  $D_{ohm} \gg D_{visc}$ , and thus  $f_{ohm}$  is expected to be close to 1. This would make our predicted  $f_{ohm}$  trend not physically noticeable. An increase of  $E_{mag}/E_{kin}$  and  $\Lambda$ , the integrated non-dimensional magnetic energy, might be in contradiction with the aforementioned scaling laws, but we show their compatibility in Sec. 3.5.

Note that the values of  $E_{mag}/E_{kin}$  that we show are below equipartition (i.e.  $0.1 < E_{mag}/E_{kin} < 0.6$  for the long  $1M_J$  sequence). This is because we analyze a volume including the non-conducting outer layer. If we restrict the energy integration within the metallic region  $r < r_m$  then  $0.25 < E_{mag}/E_{kin}|_{r < r_m} < 1.4$ . This tendency can be sensed from the radial distributions of both Fig. 4 and 7.

### 3.4. Dependence on planetary mass

We have obtained saturated models for five different masses at 5 Gyr. We directly compare only four of them, as the conductivity of the  $0.3 M_J$  model was not numerically feasible with  $\rho_{ratio} \approx 20$  (see above). The model of  $4 M_J$  is slightly under-resolved, possibly because of its higher  $Ra$  and a very little conductivity drop, which does not help stabilize the stress-free boundary conditions. We did not use higher mass models 1D models, specifically the 8 and  $12 M_J$ , due to resolution constraints that the  $E$ ,  $Ra$  combination required.

The main dimensionless diagnostics for these runs were already shown in Fig. 5. The overall trends are dictated by the increase of  $Ra$  with a decrease of  $E$  that comes with the 1D profiles themselves. Therefore, as mass increases both  $f_{dip}$  and  $f_{dip,dyn}$  decrease, while  $f_{ohm}$ ,  $\Lambda$ , and  $Rm$  increase. The energy ratio is approximately maintained.

In Fig. 7 we plot the energy spectra and radial distribution for these models. The key features are very similar to the one described above (Fig. 4). A noticeable difference is that the magnetic spectra seem to become flatter for higher masses. The sawtooth shape in the kinetic spectra diminishes with mass. This is due to the decreasing depth of the outer non-conductive layer, as hydrogen metallization pressures are reached faster. To overcome this difference and to observe whether the evolutionary trends shown in Fig. 5 did not change for other masses, we obtained saturated dynamos for the  $4 M_J$  0.5, 1 and 10 Gyr  $\rho_{ratio} \approx 100$  models. For the three of them, we obtained similar dynamos with larger equatorial jets, in other words, we recovered the tooth shape seen in the kinetic spectrum. The evolutionary trends match with the multipolar side of the  $1 M_J$  long series.

### 3.5. Evolution of the magnetic field strength at the dynamo surface

The scaling law provided by Reiners et al. (2009) gives the mean strength of the magnetic field at the dynamo surface,  $B_{dyn}$ , in terms of the mass  $M$ , luminosity  $L$  and radius  $R$  of

the sub-stellar object:

$$B_{dyn} = 4.8^{+3.2}_{-2.8} \left( \frac{M}{M_\odot} \right)^{1/6} \left( \frac{L}{L_\odot} \right)^{1/3} \left( \frac{R}{R_\odot} \right)^{7/6} \text{ kG}. \quad (15)$$

We can evaluate  $B_{dyn}$  by using the  $L(t)$ ,  $R(t)$  output from our MESA simulations (pink lines in Fig. 8).

Another slightly different estimate comes from inserting in eq. (15) the analytical expressions for  $L(t)$  and  $R(t)$  of Burrows & Liebert (1993); Burrows et al. (2001), given for sub-stellar mass solar-metallicity object:

$$L \sim 4 \cdot 10^5 L_\odot \left( \frac{1 \text{Gyr}}{t} \right)^{1.3} \left( \frac{M}{0.05 M_\odot} \right)^{2.64}, \quad (16)$$

$$R \sim 6.7 \cdot 10^4 \text{km} \left( \frac{10^5 \text{cm s}^{-2}}{g} \right)^{0.18} \left( \frac{T_{eff}}{1000 \text{K}} \right)^{0.11}. \quad (17)$$

Using these estimates, Reiners & Christensen (2010) obtained a slow decay of the dynamo magnetic field, of about one order of magnitude over around 10 Gyr. From Fig. 1 in their article, the approximate power-law relation is  $B_{dyn} \sim t^{-0.3}$  (marked with a gray line in Fig. 8).

We can then compare these methods with ours, and to do so we need to evaluate the values of  $B_{dyn}$  for our models. As mentioned above, we make use of the fact that the effective dynamo surface is located at  $r_m$ . We decided to obtain the volume average of  $E_{mag}$  over a spherical shell from  $r_m$  to some not-too-deep layer:

$$E_{mag,dyn}(q) = \frac{1}{r_m - r'_m} \int_{r'_m}^{r_m} E_{mag}(r) dr, \quad (18)$$

where  $r'_m(q) = (\chi_m - q)r_o$ , and  $E_{mag}(r)$  is obtained from the previously shown radial distributions. The shell thickness is therefore controlled by the parameter  $q$  which in turn allows us to evaluate the surface dynamo field as  $B_{dyn}(q) = \sqrt{2\mu_0 E_{mag,dyn}(q)/MV}$ . In Fig. 8 we show the estimated  $B_{dyn}$  for  $q = 0.05, 0.1, 0.15$  and  $0.2$  (colored points in Fig. 8, with the related statistical error). The best-fitting slope (dotted lines) decreases with thicker integrating regions, that is larger  $q$ . Within standard deviations, we recover the previously mentioned slope of  $\sim t^{-0.3}$  for the most uncertain slope (thinnest averaging region). The others are slightly shallower than the trends obtained by Reiners & Christensen (2010) and Reiners et al. (2009).

### 3.6. Dependence on the Prandtl numbers

To assess the impact of the assumption of constant  $Pr$  and  $Pm$ , we obtained several saturated dynamo states with  $Pr, Pm \neq 1$  for some  $1 M_J$  models. We performed runs with the 0.5, 1, and 10 Gyr which we deem enough for assessing general properties of the trends. We investigated within the following range:  $0.5 < Pm < 4$  and  $0.5 < Pr < 2$ . The results are shown in Fig. 9.

Increasing  $Pm$  can be understood as lowering  $\lambda$  while keeping  $\nu$  constant, or similarly increasing  $\nu$  with constant  $\lambda$ . Both effects lead to an increase in magnetic energy in relation to the available buoyant power. Therefore, we can see in Fig. 9 that  $Rm$  and  $\Lambda$  tend to increase with  $Pm$ , that is a more efficient dynamo mechanism (Elias-López et al. 2024). The same applies for  $E_{mag}/E_{kin}$  and  $f_{ohm}$ , as the decreasing  $\lambda$  increases both the magnetic energy percentage and the Ohmic dissipation contribution. Both surface and volumetric dipolarities see a decrease with increasing  $Pm$  which is compatible with what was found by Tsang & Jones

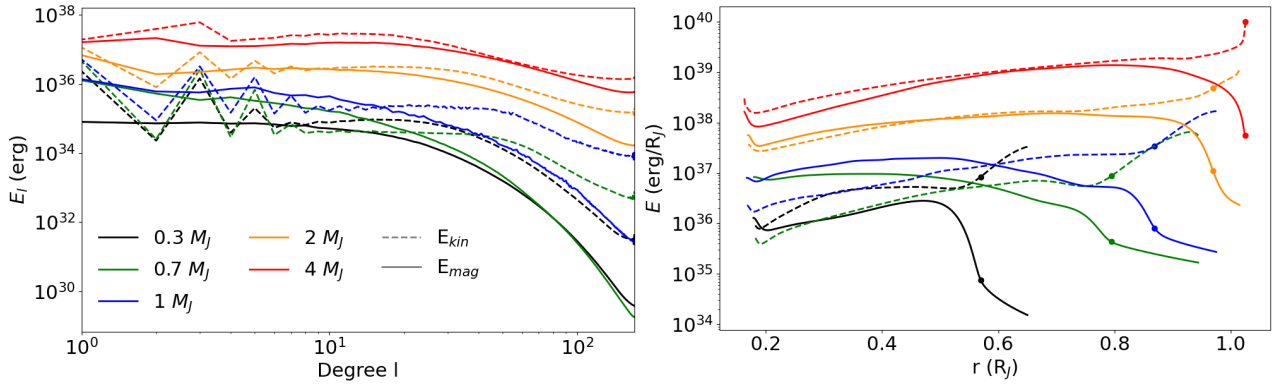


Fig. 7: Magnetic (solid) and kinetic (dashed) energy distribution over the multipole degrees  $l$  (left), and over the radius (right) for planets with different masses at 5 Gyr. The location of  $r_m$  is marked with a dot in the radial plots.

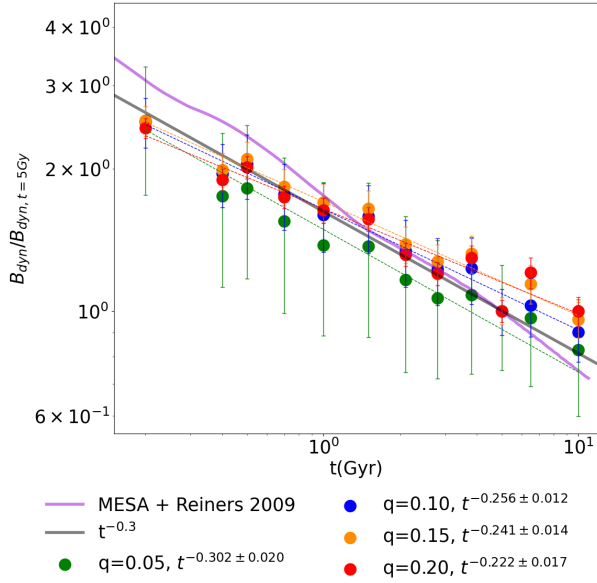


Fig. 8: Evolution of the magnetic field strength at the dynamo surface averaged in time, using the scaling laws and calculating the average value of the magnetic field over different relative thicknesses  $q$ , around  $r_m$  (green, blue, orange, red). The error bars are associated to radial variation and are larger for thinner integration shells over which we evaluate eq. 18. The dotted lines are the corresponding best-fit power laws. The solid lines indicate eq. (15) applied to our MESA output (pink), and the prediction by Reiners & Christensen (2010) (gray).

(2020): higher  $Pm$  means a less steep magnetic spectrum, or in other words less dipole-dominated.

Contrarily,  $Rm$ ,  $\Lambda$ ,  $f_{ohm}$  decrease for increasing  $Pr$ . This can be easily understood if one thinks of higher  $Pr$  as increasing values of  $\nu$  in comparison to  $\kappa$ . Higher viscosity will lead to less kinetic as well as magnetic energy, and therefore lower  $Rm$  and  $\Lambda$ . The decrease of  $f_{ohm}$  means that Ohmic dissipation becomes less important than viscous dissipation. The magnetic energy ratio,  $E_{mag}/E_{kin}$ , and both dipolarities,  $f_{dip}$  and  $f_{dip,dyn}$ , increase with  $Pr$ , as it leads to a more efficient dynamo mechanism.

With these trends in mind, we can argue how the constant  $Pr$  and  $Pm$  assumptions affect the obtained trends in Figs. 5 and 8. A slight increase of  $Pr$  is expected to happen during the long-term evolution of the planets, since, while

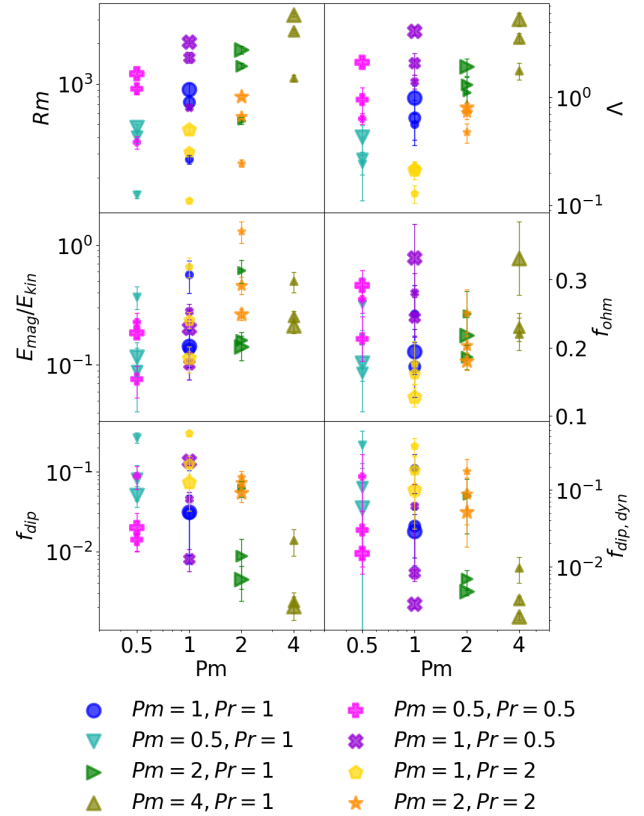


Fig. 9: Same diagnostics as in Fig. 5, shown as a function of  $Pm$ , with different values of  $Pr$ . The decreasing size of the mark indicates the increase in age (0.5, 1, 10 Gyr). Colors and shapes help distinguish evolutionary changes and are shared with Fig. 10 and 11.

it cools down, the ratio between the thermal and electrical conductivities (inversely proportional to  $Pr$ ) decreases according to the Wiedemann-Franz law, valid in the metallic region (French et al. 2012). On the contrary, viscosity and conductivity themselves are not supposed to vary appreciably with temperature (i.e. in time) (French et al. 2012; Bonitz et al. 2024). Therefore by using the trend of  $\Lambda$  with  $Pr$ , we expect that, if one considered an evolutionary change of  $Pr$ , the trend  $B_{dyn}(t)$  would be slightly steeper, possibly in even higher agreement with the Reiners & Christensen (2010) scaling law trend. However, a firm conclusion about this, using a modified setup for diffusivities and  $Pr$  evolution, is left for future work.

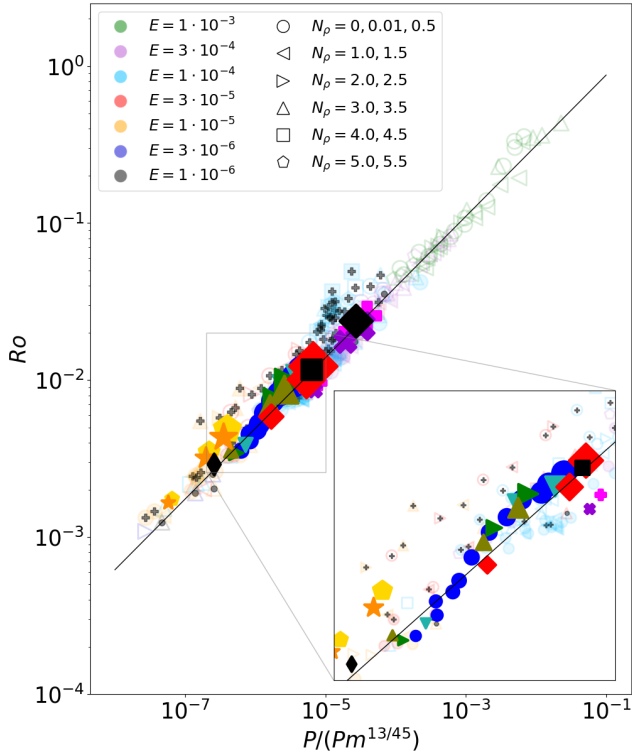


Fig. 10: Rossby number as a function of a combination of non-dimensional buoyancy power and magnetic Prandtl number. The solid line corresponds to the power law  $Ro = 2.47P^{0.45}Pm^{-0.13}$ . The semitransparent data are taken from Yadav et al. (2013) and are plotted with a similar symbol and color scheme (note that the legend is different from our runs). Filled (empty) symbols correspond to dipolar (multipolar) dynamos, where they define dipolar as  $f_{dip, l < 12}^{axi, surf} > 0.3$ . The Ekman number is color coded and the marker shape indicates the degree of density stratification, as  $N_\rho = \ln(\rho_{ratio})$ . Symbols containing a "+" have an exponentially decaying conductivity as eq. (7), and the ones carrying a dot symbol have a moderate outward decay of  $\sigma$ ,  $\nu$  and  $\kappa$ , all proportional to  $\rho(r)$ . The complete input and output set can be found in the additional data of the original article. The results of this work are superposed with the same legend as Fig. 5, and the size of the marker denotes the approximate age and mass of the planet.

In general, the evolutionary trends seen in Fig. 5 are maintained regardless of  $Pr$  and  $Pm$ .  $Rm$  decreases similarly for all sets runs. Both surface and volumetric dipolarities with time. And finally,  $E_{mag}/E_{kin}$ ,  $\Lambda$  and  $f_{ohm}$  show a different behavior depending on their dipolarity. The two most dipolar solutions ( $Pm = 1, Pr = 2$  and  $Pm = 2, Pr = 2$ ) consistently show the same behavior noted above, that is an increase of  $E_{mag}/E_{kin}$  and  $f_{ohm}$  in time, and a plateau/mild decrease of  $\Lambda$ . In contrast, the most multipolar set of Prandtl numbers ( $Pm = 4, Pr = 1$ ) shows a decrease both in  $f_{ohm}$  and  $\Lambda$  and a slight more shy increase  $E_{mag}/E_{kin}$ . The other sets of runs are consistent with a transition from multipolar to dipolar similar to Fig. 5.

### 3.7. Scaling laws

Yadav et al. (2013) used a large set of anelastic dynamo numerical solutions to derive scaling laws relating several representative dimensionless diagnostic parameters. Their

dynamos covered a large space of parameters:  $0 \leq \rho_{ratio} \leq 245$ ,  $0.1 \leq \eta \leq 0.75$ ,  $0.3 \leq Pr \leq 10$ ,  $0.2 \leq Pm \leq 20$ ,  $10^{-6} \leq E \leq 10^{-3}$  and  $2.5 \cdot 10^5 \leq Ra \leq 2.5 \cdot 10^9$ . The scattering plots shown in Fig. 10 and 11 super-impose the results of Yadav et al. (2013) with the data representing our models.

To compare our results, we need to use the inverse rotation frequency  $\Omega^{-1}$  as the time unit, and the magnetic field units of  $\Omega D \sqrt{\mu_o \rho_o}$ . The buoyancy power  $P$  is:

$$P = \frac{RaE^3}{Pr} \frac{\langle \tilde{\alpha} \tilde{T} \tilde{g} s' u_r \rangle}{M}, \quad (19)$$

where  $M$  is the dimensionless mass of the shell, listed in Table 1 for our models. In Fig. 10 we show  $Ro$  as a function of  $P/Pm^{13/45}$ . For the runs of Yadav et al. (2013), there is a clear separation between the models with constant  $\sigma$ , which lie close to the best-fitting power law (gray line), and the runs with a decaying  $\sigma$  profile near the surface, which lie slightly above but parallel to the trend. The reason is that when using a decaying  $\sigma$ , the strong jets that appear in the external non-conductive layer tend to increase the total kinetic energy, and thus  $Ro$ , for the same amount of available  $P$ . Our definition of  $Ro$  differs by a factor of  $1/\lambda$  that erases the outer jet contribution, leading to our runs lying mostly over the scaling law itself. We observe how our models representing different evolutionary stages of the planetary magnetoconvection move through this dimensionless space. This progression is parallel to the power law  $Ro = 2.47P^{0.45}Pm^{-0.13}$  and goes from higher to lower values: for a single model  $Ro$  decreases about half an order of magnitude while  $P/Pm^{13/45}$  decreases one order of magnitude (which corresponds to the 0.45 exponent). Physically, this evolution should be positioned orders of magnitude away, but if the scaling law holds, so should this trend.

We also define the Lorentz number,  $Lo$ , as the non-dimensional magnetic field strength in  $\Omega^{-1}$  time units per unit of mass. In this case  $B$  is in units of  $\Omega d \sqrt{\rho_o \mu_o}$  and we can relate the definition of  $Lo$  with  $\Lambda$ ,  $E$  and  $Pm$ :

$$Lo = \frac{B_{rms}}{\Omega d \sqrt{\rho_o \mu_o}} \frac{1}{\sqrt{M}} = \sqrt{\frac{2E_{mag}E^2}{M}}. \quad (20)$$

The other magnetic-related scaling law involves the characteristic timescale of magnetic energy dissipation  $\tau_{mag}$ , defined as the non-dimensional magnetic energy divided by the joule heat dissipation (all in units of  $\Omega^{-1}$ ):

$$\tau_{mag} = \frac{E_{mag}E^2}{P f_{ohm} M}. \quad (21)$$

In Fig. 11 we show the the scaling laws for  $Lo$  and  $\tau_{mag}$  with the same legend as Fig. 10. In Yadav et al. (2013) they find that dipolar- and multipolar-dominated solutions take similar but parallel trends. We have over-plotted our runs with the joined dipolar/multipolar branches for both scaling laws (they show them separately). As suspected from Sec. 3.3, our series evolves from the multipolar to the dipolar branch in both diagrams, but it can be more clearly appreciated in the  $\tau_{mag}$  plot. This is also an argument in favor for this possible multipolar to dipolar transition.

Note that the power law relations shown above are purely fits obtained from Yadav et al. (2013). The velocity scaling of  $Ro \propto P^\alpha$  with  $\alpha$  somewhat larger than 0.4 has been theoretically justified by force balances by some authors (Aubert et al. 2001; Davidson 2013; Starchenko & Jones 2002), but non has derived a  $Pm$  dependence. Similarly, there are some discussion for  $\tau_{mag} \propto Ro^\alpha$  where

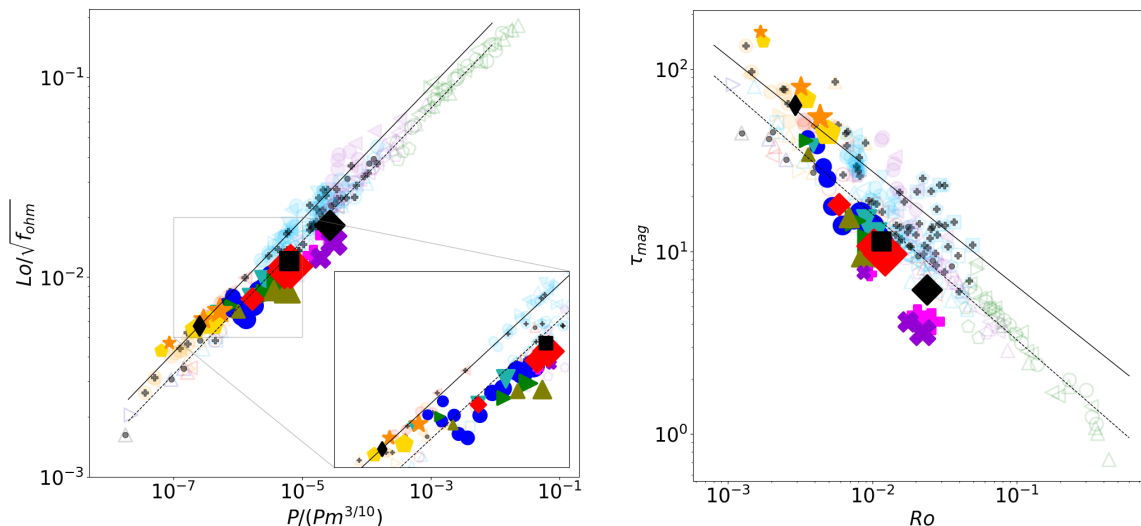


Fig. 11: On the left: Lorentz number corrected for the fraction of Ohmic dissipation as a function of a combination of non-dimensional buoyancy power and magnetic Prandtl number. The scaling relations are  $Lo f_{ohm}^{-1/2} = AP^{1/3} Pm^{1/10}$ , where  $A$  is 0.9 or 0.7 for dipolar and multipolar dynamos, respectively. Yadav et al. (2013) found that the value  $f_{dip,l < 12}^{axi,surf} > 0.3$  divides the data in dipolar and multipolar, and these two types of runs are best fitted separately. On the right: characteristic timescale of magnetic energy dissipation as a function of Rossby number. The scaling relations are  $\tau_{mag,dip} = 1.51 Ro^{-0.63}$  and  $\tau_{mag,mulip} = 0.67 Ro^{-0.69}$ . The legend is the same as for Fig. 10.

$\alpha \lesssim -1$  (Christensen & Tilgner 2004; Stelzer & Jackson 2013) or  $\alpha \sim -0.75$  (Davidson 2013). And finally, if the magnetic field is only a function of power, dimensional arguments dictate that it must depend on the cubic root of the power, that is  $Lo \propto P^{1/3}$  (Kunnen et al. 2010; Christensen et al. 2009; Davidson 2013).

#### 4. Conclusions

In this work, we used 1D thermodynamical profiles taken from gas giant evolutionary models to obtain sequences of 3D MHD spherical shell dynamo models. From the public code MESA, we obtained the radial hydrostatic profiles for different mass planets at different stages of evolution:  $0.3 M_J < M_p < 4 M_J$  and  $0.2 \text{ Gyr} < t < 10 \text{ Gyr}$ , respectively. From the evolutionary tracks, we derived the trends for the dynamo parameters. Using the radial profiles as the background state, we solved the resistive MHD equations under the anelastic approximation with a pseudospectral spherical shell code, MagIC. We obtained saturated dynamo solutions and we interpret them as different snapshots of planetary magnetoconvection evolution during its long-term evolution.

For our longest set of runs representing different evolutionary times of a  $1 M_J$  planet, we find a transition from a multipolar to dipolar dominated dynamo regime. Within a regime, very few snapshots are enough to generally assess the behavior that could not be straightforwardly derived from scaling laws. As the planet evolves and cools down, we obtained a steady decrease for  $Rm$ ,  $P$ , and  $Ro$ , as well as an increase in volumetric and surface dipolarities. We find that for multipolar dynamo solutions  $\Lambda$ ,  $f_{ohm}$  and  $E_{mag}/E_{kin}$  decrease with time, whereas for more dipolar dynamos they increase. These quantities are a proxy for the magnetic field energy, the dynamics of the power dissipation, and the energy ratio respectively. Such trends hold for different Prandtl numbers, as well as for the  $4 M_J$  models.

One of the major results is the evolution of the magnetic field intensity at the dynamo surface, within a given age sequence. We obtained a magnetic field decay (Fig. 8) which is roughly compatible with existing estimates but with a different methodology, based on a sequence of realistic backgrounds. These results can be representative of the real long-term evolution if the trends (in time, or mass) of the physical solutions within a given sequence hold also for a realistic (but computationally unfeasible) range of dynamo numbers. This is the major intrinsic caveat of any dynamo study, but our results are compatible with previously proposed scaling laws for the magnetic field intensity.

Comparing this work with the anelastic scaling laws of Yadav et al. (2013) we show how one planetary dynamo evolves in the parameter space set by a combination of dimensionless diagnostics. Our sequences transition from multipolar-dominated to dipolar-dominated solutions. Taking Jupiter and Saturn dynamos as an example, we expect planetary dynamos to follow the dipolar trends at an advanced evolutionary age. According to these results, multipolar gas giant dynamos could exist in the early stages of magnetoconvection planets which would then evolve to a dipolar regime. Another possibility would be that they are already born in a dipole-dominated parameter space region.

Additionally, in the sequences, we have considered the values of  $Pr$  and  $Pm$  fixed, and the values of  $Ra$  and  $E$  changing only due to the evolving values of  $\Delta T$ ,  $T_o$ , and the shell thickness. Taking into account a possible decrease in  $Pr$ , we would expect a more steep decrease of the magnetic field at the dynamo surface, thus into more accordance with the scaling laws. In the presence of non-negligible external torques that would spin down the planet (for instance, tidal frictions with large satellites),  $E$  would (slightly) increase, which, for the trends seen in our sets, would lead to a (slight) enhancement of the slow magnetic decay. We leave this fine-tuned exploration for a follow-up work.

By using the conservative definition of a cold gas giant by setting their equilibrium temperature of less than 270 K,

there are more than 200 candidates for which these evolutionary trends could be applied. The effects of inflation and tidal synchronization are not relevant up to orbital distances of the order of 0.1 AU. Thus, weakly to moderately irradiated gas giants can also follow these evolutionary changes. Finally, the methodology used in this study can be applied also to brown dwarfs and rapidly rotating stars with similar low- $Ro$  dynamos that follow Christensen et al. (2009) scaling laws.

*Acknowledgements.* AEL and CSG's work has been carried out within the framework of the doctoral program in Physics of the Universitat Autònoma de Barcelona. AEL, DV, CSG, and TA are supported by the European Research Council (ERC) under the European Union's Horizon 2020 research and innovation program (ERC Starting Grant "IMAGINE" No. 948582, PI: DV). FDS acknowledges support from a Marie Curie Action of the European Union (Grant agreement 101030103). AEL, FDS, DV, CSG, and TA acknowledge the support from the "María de Maeztu" award to the Institut de Ciències de l'Espai (CEX2020-001058-M). We acknowledge the use of the MareNostrum BSC supercomputer of the Spanish Supercomputing Network, via projects RES/BSC Call AECT-2024-2-0011 (PI AEL), AECT-2023-2-0034 (PI FDS), AECT-2024-2-0003 (PI FDS). We are grateful to Thomas Gastine, for the usage guidance of MagIC.

## References

- Ardes, M., Busse, F. H., & Wicht, J. 1997, *Physics of the Earth and Planetary Interiors*, 99, 55
- Aubert, J., Brito, D., Nataf, H.-C., Cardin, P., & Masson, J.-P. 2001, *Physics of the Earth and Planetary Interiors*, 128, 51
- Backus, G., Parker, R., & Constable, C. 1996
- Batygin, K. 2018, *AJ*, 155, 178
- Batygin, K. & Stevenson, D. J. 2010, *The Astrophysical Journal Letters*, 714, L238
- Bodenheimer, P., Lin, D. N. C., & Mardling, R. A. 2001, *ApJ*, 548, 466
- Bonitz, M., Vorberger, J., Bethkenhagen, M., et al. 2024, *arXiv e-prints*, arXiv:2405.10627
- Braginsky, S. I. & Roberts, P. H. 1995, *Geophysical and Astrophysical Fluid Dynamics*, 79, 1
- Burrows, A., Hubbard, W. B., Lunine, J. I., & Liebert, J. 2001, *Reviews of Modern Physics*, 73, 719
- Burrows, A. & Liebert, J. 1993, *Reviews of Modern Physics*, 65, 301
- Cao, H., Dougherty, M. K., Hunt, G. J., et al. 2023, *arXiv e-prints*, arXiv:2301.02756
- Christensen, U. R. & Aubert, J. 2006, *Geophysical Journal International*, 166, 97
- Christensen, U. R., Aubert, J., Cardin, P., et al. 2001, *Physics of the Earth and Planetary Interiors*, 128, 25
- Christensen, U. R., Holzwarth, V., & Reiners, A. 2009, *Nature*, 457, 167
- Christensen, U. R. & Tilgner, A. 2004, *Nature*, 429, 169
- Christensen, U. R. & Wicht, J. 2007, in *Core Dynamics*, ed. G. Schubert, Vol. 8, 245–282
- Connerney, J. E. P., Timmins, S., Oliverson, R. J., et al. 2022, *Journal of Geophysical Research: Planets*, 127, e2021JE007055, e2021JE007055
- Davidson, P. A. 2013, *Geophysical Journal International*, 195, 67
- Duarte, L. D., Gastine, T., & Wicht, J. 2013, *Physics of the Earth and Planetary Interiors*, 222, 22
- Duarte, L. D., Wicht, J., & Gastine, T. 2018, *Icarus*, 299, 206
- Elias-López, A., Del Sordo, F., & Viganò, D. 2024, *A&A*, 690, A77
- Fortney, J. J., Dawson, R. I., & Komacek, T. D. 2021, *Journal of Geophysical Research (Planets)*, 126, e06629
- French, M., Becker, A., Lorenzen, W., et al. 2012, *The Astrophysical Journal Supplement Series*, 202, 5
- Gastine, T., Duarte, L., & Wicht, J. 2012, *A&A*, 546, A19
- Gastine, T. & Wicht, J. 2012, *Icarus*, 219, 428
- Gastine, T. & Wicht, J. 2021, *Icarus*, 368, 114514
- Gastine, T., Wicht, J., Duarte, L. D. V., Heimpel, M., & Becker, A. 2014, *Geophys. Res. Lett.*, 41, 5410
- Gilman, P. A. & Glatzmaier, G. A. 1981, *ApJ*, 45, 335
- Glatzmaier, G. A. 1984, *Journal of Computational Physics*, 55, 461
- Glatzmaier, G. A. 1985a, *ApJ*, 291, 300
- Glatzmaier, G. A. 1985b, *Geophysical and Astrophysical Fluid Dynamics*, 31, 137
- Glatzmaier, G. A. & Coe, R. S. 2007, in *Core Dynamics*, ed. G. Schubert, Vol. 8, 283–297
- Grote, E., Busse, F. H., & Tilgner, A. 2000, *Physics of the Earth and Planetary Interiors*, 117, 259
- Guillot, T., Burrows, A., Hubbard, W. B., Lunine, J. I., & Saumon, D. 1996, *ApJ*, 459, L35
- Gómez-Pérez, N., Heimpel, M., & Wicht, J. 2010, *Physics of the Earth and Planetary Interiors*, 181, 42
- Jones, C., Boronski, P., Brun, A., et al. 2011, *Icarus*, 216, 120
- Jones, C. A. 2011, *Annual Review of Fluid Mechanics*, 43, 583
- Jones, C. A. 2014, *Icarus*, 241, 148
- Klepeis, J. E., Schafer, K. J., Barbee, T. W., I., & Ross, M. 1991, *Science*, 254, 986
- Komacek, T. D. & Youdin, A. N. 2017, *ApJ*, 844, 94
- Kumar, S., Poser, A. J., Schöttler, M., et al. 2021, *Phys. Rev. E*, 103, 063203
- Kunnen, R. P. J., Geurts, B. J., & Clercx, H. J. H. 2010, *Journal of Fluid Mechanics*, 642, 445
- Lantz, S. R. & Fan, Y. 1999, *ApJS*, 121, 247
- Lowes, F. J. 1974, *Geophysical Journal*, 36, 717
- Mauersberger, P. 1956, *Zeitschrift Angewandte Mathematik und Mechanik*, 36, 398
- Nettelmann, N. 2015, *Contributions to Plasma Physics*, 55, 116
- Nettelmann, N., Fortney, J. J., Moore, K., & Mankovich, C. 2015, *MNRAS*, 447, 3422
- Paxton, B., Bildsten, L., Dotter, A., et al. 2011, *ApJS*, 192, 3
- Paxton, B., Cantiello, M., Arras, P., et al. 2013, *ApJS*, 208, 4
- Paxton, B., Marchant, P., Schwab, J., et al. 2015, *ApJS*, 220, 15
- Paxton, B., Schwab, J., Bauer, E. B., et al. 2018, *ApJS*, 234, 34
- Paxton, B., Smolec, R., Schwab, J., et al. 2019, *ApJS*, 243, 10
- Perna, R., Menou, K., & Rauscher, E. 2010, *ApJ*, 719, 1421
- Reiners, A., Basri, G., & Christensen, U. R. 2009, *ApJ*, 697, 373
- Reiners, A. & Christensen, U. R. 2010, *A&A*, 522, A13
- Sasaki, Y., Takehiro, S.-i., Kuramoto, K., & Hayashi, Y.-Y. 2011, *Physics of the Earth and Planetary Interiors*, 188, 203
- Saumon, D., Chabrier, G., & van Horn, H. M. 1995, *ApJS*, 99, 713
- Schaeffer, N., Jault, D., Nataf, H. C., & Fournier, A. 2017, *Geophysical Journal International*, 211, 1
- Schrinner, M., Petitdemange, L., & Dormy, E. 2012, *ApJ*, 752, 121
- Schubert, G. & Soderlund, K. M. 2011, *Physics of the Earth and Planetary Interiors*, 187, 92
- Schwaiger, T., Gastine, T., & Aubert, J. 2019, *Geophysical Journal International*, 219, S101
- Simitev, R. & Busse, F. H. 2003, *New Journal of Physics*, 5, 97
- Simitev, R. D. & Busse, F. H. 2009, *EPL (Europhysics Letters)*, 85, 19001
- Starchenko, S. V. & Jones, C. A. 2002, *Icarus*, 157, 426
- Stelzer, Z. & Jackson, A. 2013, *Geophysical Journal International*, 193, 1265
- Tan, X. & Komacek, T. D. 2019, *ApJ*, 886, 26
- Thorngren, D. P. & Fortney, J. J. 2018, *AJ*, 155, 214
- Tsang, Y.-K. & Jones, C. A. 2020, *Earth and Planetary Science Letters*, 530, 115879
- Wicht, J., Gastine, T., & Duarte, L. D. V. 2019a, *Journal of Geophysical Research (Planets)*, 124, 837
- Wicht, J., Gastine, T., Duarte, L. D. V., & Dietrich, W. 2019b, *A&A*, 629, A125
- Yadav, R. K., Cao, H., & Bloxham, J. 2022, *The Astrophysical Journal*, 940, 185
- Yadav, R. K., Gastine, T., Christensen, U. R., & Duarte, L. D. V. 2013, *ApJ*, 774, 6
- Yadav, R. K., Gastine, T., Christensen, U. R., Wolk, S. J., & Poppenhaeger, K. 2016, *Proceedings of the National Academy of Science*, 113, 12065
- Zaire, B., Jouve, L., Gastine, T., et al. 2022, *MNRAS*, 517, 3392
- Zhang, K. K. & Busse, F. H. 1987, *Geophysical and Astrophysical Fluid Dynamics*, 39, 119

## Appendix A: Sensitivity on the density ratio

To evaluate how the external cut applied to the 1D MESA profile influences the overall dynamo behavior, we compare the dynamo corresponding to  $\rho_{\text{ratio}} \approx 10, 20, 40, 100$  for the  $1M_J$  1 Gyr model keeping the same 3D resolution of  $(N_r, N_\theta, N_\phi) = (289, 256, 512)$ . By looking at the spectra, the model with  $\rho_{\text{ratio}} \approx 100$  seems slightly under-resolved (there is an overall drop of only 1 order of magnitude, less than what indicates a large enough grid), but the overall quantities seem to follow the same trend as with the other distinct  $\rho_{\text{ratio}}$  models. We could not explore properly higher values of  $\rho_{\text{ratio}} \gtrsim 200$ , due to the excessive resolution required. In Table A.1 we show the different diagnostics.

Table A.1: General outputs for the  $1M_J$  1 Gyr models with different densities.

$\rho_{\text{ratio}}$	10.0	19.8	39.8	97.9
$Rm$	1097	732	461	301
$Ro$	$1.35 \cdot 10^{-2}$	$8.20 \cdot 10^{-3}$	$4.98 \cdot 10^{-3}$	$3.16 \cdot 10^{-3}$
$\Lambda$	1.87	0.67	0.172	0.072
$P$	$8.74 \cdot 10^{10}$	$7.16 \cdot 10^{10}$	$5.10 \cdot 10^{10}$	$3.83 \cdot 10^{10}$
$E_{\text{mag}}/E_{\text{kin}}$	0.207	0.146	0.090	0.087
$f_{\text{ohm}}$	0.283	0.190	0.101	0.066
$E_{\text{kin}}$ (code)	$1.48 \cdot 10^7$	$1.62 \cdot 10^7$	$1.54 \cdot 10^7$	$1.58 \cdot 10^7$
$E_{\text{kin}}$ (erg)	$1.39 \cdot 10^{38}$	$9.3 \cdot 10^{37}$	$4.80 \cdot 10^{37}$	$1.82 \cdot 10^{37}$
$E_{\text{mag}}$ (code)	$3.07 \cdot 10^6$	$2.37 \cdot 10^6$	$1.38 \cdot 10^6$	$1.37 \cdot 10^5$
$E_{\text{mag}}$ (erg)	$2.90 \cdot 10^{37}$	$1.37 \cdot 10^{37}$	$4.32 \cdot 10^{36}$	$1.58 \cdot 10^{36}$
$f_P$ (%)	0.18	0.0033	0.31	0.43

Generally, many of the dimensionless quantities are affected by the value of  $\rho_{\text{ratio}}$ . Except for the  $\rho_{\text{ratio}} \approx 100$  model, the overall kinetic energy seems to plateau (in code units). However, since a dominant fraction of the kinetic energy is located in the non-conductive outer layers (see Fig. 4), all magnitudes containing  $u_{rms}$  may differ substantially. As we capture more density ratio, the aforementioned zonal flows gain importance and compete against the magnetic field in the interior affecting the overall dynamics. For example, even though  $Ra$  increases, the total buoyant power,  $P$ , decreases because it depends only on  $u_r$ . Similarly,  $Rm$  and  $Ro$  also decrease even though they depend on  $u_{rms}$ . This is due to the decreasing dimensionless diffusivity  $1/\lambda$ , which erases the zonal flow contribution and only captures the suppression of the internal convection with higher  $\rho_{\text{ratio}}$ . Consequently, the Elsasser number  $\Lambda$  and  $E_{\text{mag}}$ , also  $\rho_{\text{ratio}}$  also decrease for the same suppression reasons. Correcting factors for the dimensionless mass  $M$  and volume  $V$  do not mitigate the differences among the  $\rho_{\text{ratio}}$  series.

To overcome this systematic effect, we tend to compare models with a similar  $\rho_{\text{ratio}}$ , independently of the mass and age of the model. For most models, we choose  $\rho_{\text{ratio}} \approx 20$ , as it is more computationally feasible but still has a relevant non-conductive outer layer where the zonal jet develops. This restriction allows us to analyze the different saturated models for an evolutionary sequence.

## Appendix B: Initial conditions from previous models

To reduce the computational resources and avoid starting each model with random initial conditions, we have usually employed already saturated solutions as initial conditions for other models. As we are interpreting the different models as stages in planetary evolution an obvious choice would be to use, for example, the saturated state of the  $1M_J$  0.5

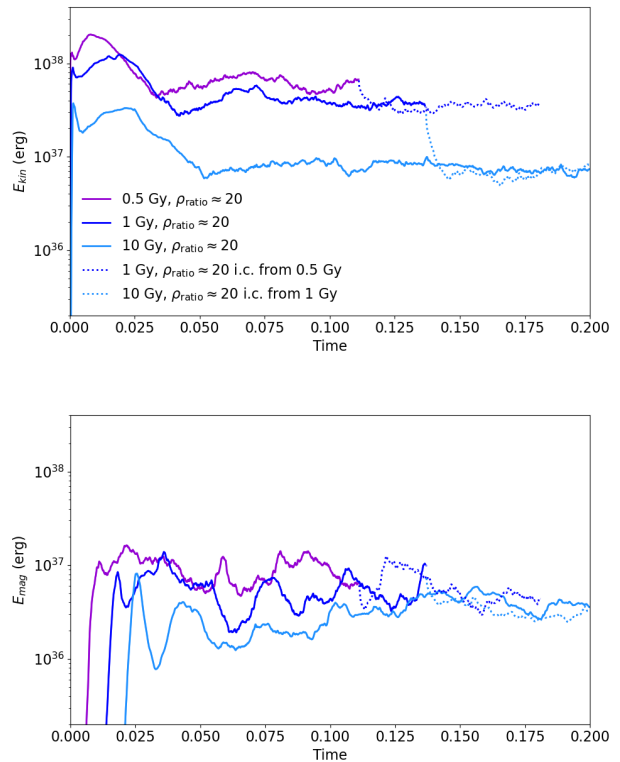


Fig. B.1: Kinetic (top) and magnetic (bottom) energy evolution time series for the  $1M_J$  models at 3 different ages (different colors). Solid lines are simulations starting from a  $\mathbf{u} = 0$  initial conditions, while the dotted lines take as initial condition a snapshot of the saturated solution of another model. Time is in viscous units.

Gyr model as initial conditions for the  $M_J$  0.7 Gyr, and so on.

As a proof of concept, we made two tests: we used the final saturated state of a 0.5 Gyr model as initial conditions for a 1 Gyr model, and the same for a 1 Gyr and 10 Gyr models. In Fig. B.1 we show the kinetic and magnetic energy time series for this transitions. The steady states reached are indistinguishable, that is one cannot discern from the spectra, radial distribution, or final diagnostics in which initial conditions were used. The only quantities that showed a noticeable difference are the dipolarity indicators ( $f_{\text{dip}}$ ), but they are within one standard deviation from each other. To obtain satisfactorily similar means much longer computing times would be probably required. Overall, there is convergence, starting from different initial conditions.

The activation of convection, followed by the dynamo kinematic phase and finally to the saturated phase where Lorentz forces become relevant is a lengthy computation. Starting from an already saturated solution not too far from the expected one highly reduces by more than a factor of 5 the computing time needed to reach the new steady state. Thus in most of all models, we have used a high  $Ra$  model as initial conditions, specifically the saturated  $1M_J$  0.5 Gyr model with  $Pm = Pr = 1$ .

## Appendix C: Spectral-radial distributions and dynamo surface definition

To compare our results with (Tsang & Jones 2020), we obtained the spectral-radial energy distribution. In the top



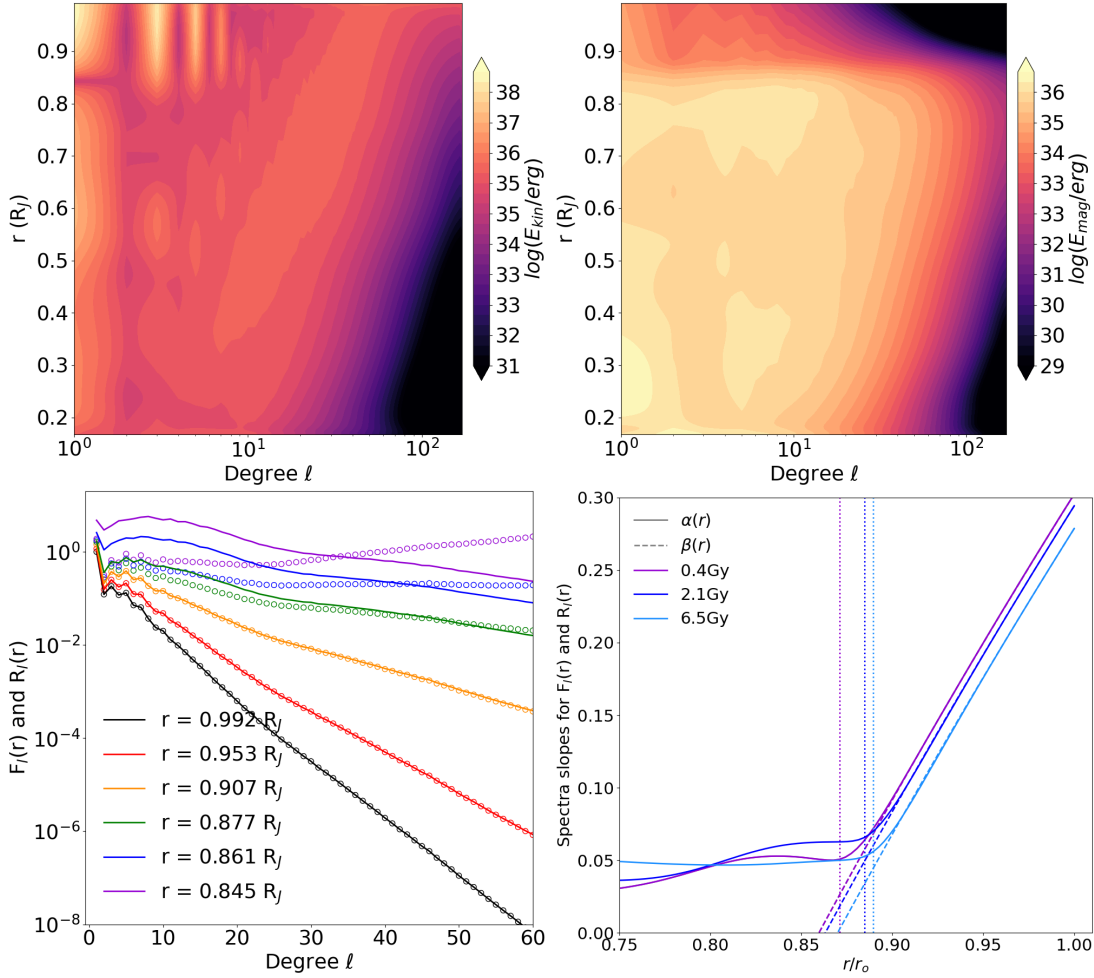


Fig. C.1: *Top*: Spectral-radial kinetic (left) and magnetic (central) energy distributions of the  $1 M_J$  2.1 Gyr model. *Bottom left*: Lowes spectra  $R_l(r)$  (circles) superimposed with  $F_l(r)$  (solid lines) at different depths for the saturated dynamo solution of the same model. *Bottom right*: Spectral slopes at different dimensionless radial depths for the same runs as Fig. 4. The vertical lines are their respective  $r_m$ .

panel of Fig. C.1 we show these spectra for the saturated  $1 M_J$  2.1 Gyr model. The radial integration of both spectra is already shown in Fig. 4. It can be observed that the radially dependent magnetic energy spectra,  $F_l(r)$ , decay rapidly for  $r > r_m = 0.88 R_J$ . At the same region, the kinetic spectra start showing the equatorial jet pattern.

In the region where  $\mathbf{J} = 0$ , we define the scalar potential  $V$ , for which  $\mathbf{B} = -\nabla V$ , with its usual spherical expansion:

$$V \equiv a \sum_{l=1}^{l_{max}} \left(\frac{a}{r}\right)^{l+1} \sum_{m=0}^l P_l^m(\cos\theta) \left[ g_l^m \cos(m\phi) + h_l^m \sin(m\phi) \right], \quad (\text{C.1})$$

where  $a$  is taken as the planetary radius,  $P_l^m$  are the Schmidt semi-normalized associated Legendre polynomials, and the Gauss coefficients  $g_l^m$  and  $h_l^m$  are obtained from measurements. Then the Lowes spectrum (Mauersberger 1956; Lowes 1974) on the planetary surface is defined as:

$$R_l(a) \equiv (l+1) \sum_{m=0}^l \left[ (g_l^m)^2 + (h_l^m)^2 \right]. \quad (\text{C.2})$$

For any other radii, each degree  $l$  has a different contribution as they decay differently with distance  $r$ :

$$R_l(r) = \left(\frac{a}{r}\right)^{2l+4} R_l(a). \quad (\text{C.3})$$

This expression gives the Lowes spectrum in the interior of the planet, i.e. the downward extrapolation which would be valid in the absence of electrical current (potential field). Therefore, we expect to have Lowes spectra only outside the dynamo surface, since inside it  $\mathbf{B}$  stops being potential. Moreover, from equipartition reasons, it is usually assumed that the magnetic field in the dynamo region is equally distributing among different scales until the diffusive scale ('white source hypothesis', Backus et al. 1996). A flat spectrum at the dynamo surface would imply that at the planetary surface, there will be a linear relation  $\log_{10} R_l(r) \sim -\beta(r)$ . For our saturated dynamo solutions, we define the Lowes spectrum as the magnetic spectra at the outermost radius, where we impose potential boundary conditions:

$$R_l(r_o) = F_l(r_o).$$

On the bottom left panel of Fig. C.1 we show both  $R_l(r)$  and  $F_l(r)$  at different radii for one specific saturated solution. The black line corresponds to  $r_o$  and the others are at different depths. At some specific depth  $R_l(r)$  stops being similar to  $F_l(r)$  and even has an unphysical negative slope. The Lowes radius is defined where  $\beta(r) = 0$  and it is usually taken as the depth where the dynamo starts. As (Tsang & Jones 2020) noted,  $R_l(r)$  is already quite different from  $F_l(r)$  at such radius. To surpass this discrepancy, they similarly defined the spectra slope for  $F_l(r)$ , i.e.  $\log_{10} F_l(r) \sim -\alpha(r)$ .

The slope  $\alpha(r)$  is almost the same as  $\beta(r)$  outside the dynamo region but becomes more or less flat at positive values inside. They argue that radius where  $\alpha(r)$  and  $\beta(r)$  show a discrepancy is where the effective dynamo surface is.

We similarly obtained the spectra slopes  $\alpha(r)$  and  $\beta(r)$  by a least square minimization between multipoles 10 and 50, which is the region where spectra are exponential and have not reached the dissipation scales set by our resolution. In the bottom right panel of Fig. C.1 we show the resulting spectra slopes, for the same models shown in Fig. 4. For some of our models, we do not obtain a flat spectrum inside, but if we take the average value of  $\alpha(r)$  in the dynamo region and interpolate it for the decaying outer part, we obtain values very similar to the ones of  $r_m$ , shown as vertical lines. Therefore, we can safely assume that the radial position where the conductivity starts the exponential decay,  $r_m$ , is a good definition as the dynamo surface for our models.

#### **Appendix D: Diagnostics for all the models**

In the Table D.1 we show the output parameters graphically shown in Figs. 5, 9.

Table D.1: Quantitative details of all models of Table 1, which was focused on the background setup. Here we show, for all of them the input dynamo numbers ( $E$  and  $Ra$  fixed as in Table 1, and the Prandtl numbers  $Pm$ ,  $Pr$ ), and the diagnostics:  $\Lambda$ ,  $E_{mag}$  (in code units),  $E_{kin}$  (in code units), dipolarity  $f_{dip}$ , Ohmic fraction  $f_{ohm}$ , buoyancy power  $P_\nu$ , power imbalance  $f_P$ . The values are time-averaged. The typical standard deviations, here omitted for the sake of space, are shown as error bars in Figs. 5, 9.

Model	$\rho_{ratio}$	$E$	$Ra$	$Pm$	$Pr$	$Rm$	$\Lambda$	$E_{mag}$	$E_{kin}$	$f_{dip}$	$f_{ohm}$	$P_\nu$	$f_P(\%)$
$1M_J$ 1 Gyr	10.0	$1.23 \cdot 10^{-5}$	$7.92 \cdot 10^8$	1	1	1092	1.87	$3.07 \cdot 10^6$	$1.48 \cdot 10^7$	0.0057	0.283	$8.74 \cdot 10^{10}$	0.18
	39.8	$1.08 \cdot 10^{-5}$	$1.10 \cdot 10^9$	1	1	461	0.172	$1.38 \cdot 10^6$	$1.54 \cdot 10^7$	0.053	0.101	$5.10 \cdot 10^{10}$	0.31
	97.9	$1.05 \cdot 10^{-5}$	$1.20 \cdot 10^9$	1	1	301	0.072	$1.37 \cdot 10^6$	$1.58 \cdot 10^7$	0.041	0.066	$3.83 \cdot 10^{10}$	0.43
$1M_J$ 0.2 Gyr	19.8	$1.01 \cdot 10^{-5}$	$1.63 \cdot 10^9$	1	1	1107	1.38	$5.42 \cdot 10^6$	$3.44 \cdot 10^7$	0.0271	0.235	$2.123 \cdot 10^{11}$	2.4
$1M_J$ 0.4 Gyr	19.9	$1.08 \cdot 10^{-5}$	$1.27 \cdot 10^9$	1	1	956	0.99	$3.8 \cdot 10^6$	$3.13 \cdot 10^7$	0.028	0.197	$1.49 \cdot 10^{11}$	0.45
$1M_J$ 0.5 Gyr	19.6	$1.08 \cdot 10^{-5}$	$1.22 \cdot 10^9$	1	1	904	0.987	$3.7 \cdot 10^6$	$2.56 \cdot 10^7$	0.031	0.194	$1.29 \cdot 10^{11}$	0.22
$1M_J$ 0.7 Gyr	19.8	$1.12 \cdot 10^{-5}$	$1.05 \cdot 10^9$	1	1	829	0.71	$2.58 \cdot 10^6$	$2.54 \cdot 10^7$	0.028	0.176	$9.27 \cdot 10^{10}$	0.31
$1M_J$ 1 Gyr	19.8	$1.12 \cdot 10^{-5}$	$9.81 \cdot 10^8$	1	1	734	0.649	$2.31 \cdot 10^6$	$1.68 \cdot 10^7$	0.030	0.172	$7.36 \cdot 10^{10}$	0.025
$1M_J$ 1.5 Gyr	19.6	$1.15 \cdot 10^{-5}$	$8.78 \cdot 10^8$	1	1	641	0.385	$1.32 \cdot 10^6$	$1.22 \cdot 10^7$	0.0267	0.141	$5.42 \cdot 10^{10}$	0.062
$1M_J$ 2.1 Gyr	19.9	$1.18 \cdot 10^{-5}$	$7.87 \cdot 10^8$	1	1	525	0.44	$1.29 \cdot 10^6$	$8.61 \cdot 10^6$	0.045	0.191	$4.10 \cdot 10^{10}$	0.066
$1M_J$ 2.8 Gyr	19.9	$1.20 \cdot 10^{-5}$	$7.33 \cdot 10^8$	1	1	439	0.490	$1.52 \cdot 10^6$	$7.1 \cdot 10^6$	0.104	0.216	$3.32 \cdot 10^{10}$	0.18
$1M_J$ 3.5 Gyr	19.9	$1.21 \cdot 10^{-5}$	$6.71 \cdot 10^8$	1	1	400	0.39	$1.85 \cdot 10^6$	$6.16 \cdot 10^6$	0.114	0.207	$2.93 \cdot 10^{10}$	0.26
$1M_J$ 5 Gyr	19.9	$1.23 \cdot 10^{-5}$	$6.22 \cdot 10^8$	1	1	370	0.51	$1.94 \cdot 10^6$	$4.89 \cdot 10^6$	0.130	0.232	$2.32 \cdot 10^{10}$	0.20
$1M_J$ 6.5 Gyr	19.7	$1.28 \cdot 10^{-5}$	$5.52 \cdot 10^8$	1	1	323	0.53	$2.57 \cdot 10^6$	$4.40 \cdot 10^6$	0.114	0.247	$2.15 \cdot 10^{10}$	0.079
$1M_J$ 10 Gyr	20.0	$1.30 \cdot 10^{-5}$	$4.97 \cdot 10^8$	1	1	274	0.558	$2.08 \cdot 10^6$	$3.65 \cdot 10^6$	0.130	0.250	$1.51 \cdot 10^{10}$	0.043
$1M_J$ 0.5 Gyr	19.6	$1.08 \cdot 10^{-5}$	$1.22 \cdot 10^9$	0.5	1	514	0.41	$3.0 \cdot 10^6$	$3.2 \cdot 10^7$	0.076	0.228	$1.335 \cdot 10^{11}$	0.16
	19.6	$1.08 \cdot 10^{-5}$	$1.22 \cdot 10^9$	2	1	1790	1.93	$3.50 \cdot 10^6$	$2.47 \cdot 10^7$	0.0045	0.218	$1.32 \cdot 10^{11}$	5.4
	19.6	$1.08 \cdot 10^{-5}$	$1.22 \cdot 10^9$	4	1	3250	5.30	$4.86 \cdot 10^6$	$2.27 \cdot 10^7$	0.00204	0.331	$1.40 \cdot 10^{11}$	53
	19.6	$1.08 \cdot 10^{-5}$	$1.22 \cdot 10^9$	0.5	0.5	1190	2.11	$1.50 \cdot 10^7$	$8.10 \cdot 10^7$	0.020	0.292	$5.78 \cdot 10^{11}$	6
	19.6	$1.08 \cdot 10^{-5}$	$1.22 \cdot 10^9$	1	0.5	2050	4.11	$1.46 \cdot 10^7$	$7.16 \cdot 10^7$	0.137	0.332	$5.66 \cdot 10^{11}$	11
	19.6	$1.08 \cdot 10^{-5}$	$1.22 \cdot 10^9$	1	2	454	0.213	$8.7 \cdot 10^5$	$7.62 \cdot 10^6$	0.073	0.127	$2.84 \cdot 10^{10}$	0.086
	19.6	$1.08 \cdot 10^{-5}$	$1.22 \cdot 10^9$	2	2	803	0.803	$1.63 \cdot 10^6$	$6.12 \cdot 10^6$	0.054	0.180	$3.07 \cdot 10^{10}$	0.22
$1M_J$ 1 Gyr	19.8	$1.12 \cdot 10^{-5}$	$9.81 \cdot 10^8$	0.5	1	440	0.25	$1.81 \cdot 10^6$	$2.4 \cdot 10^7$	0.093	0.153	$7.57 \cdot 10^{10}$	0.061
	19.8	$1.12 \cdot 10^{-5}$	$9.81 \cdot 10^8$	2	1	1360	1.31	$2.33 \cdot 10^6$	$1.45 \cdot 10^7$	0.0088	0.186	$7.57 \cdot 10^{10}$	1.36
	19.8	$1.12 \cdot 10^{-5}$	$9.81 \cdot 10^8$	4	1	2460	3.52	$3.17 \cdot 10^6$	$1.25 \cdot 10^7$	0.00236	0.230	$7.98 \cdot 10^{10}$	20.9
	19.8	$1.12 \cdot 10^{-5}$	$9.81 \cdot 10^8$	0.5	0.5	918	0.95	$6.6 \cdot 10^6$	$8.7 \cdot 10^7$	0.0141	0.213	$3.08 \cdot 10^{11}$	0.65
	19.8	$1.12 \cdot 10^{-5}$	$9.81 \cdot 10^8$	1	0.5	164	2.07	$7.2 \cdot 10^6$	$7.1 \cdot 10^7$	0.0081	0.245	$3.18 \cdot 10^{11}$	1.54
	19.8	$1.12 \cdot 10^{-5}$	$9.81 \cdot 10^8$	1	2	310	0.221	$9.1 \cdot 10^5$	$3.83 \cdot 10^6$	0.124	0.162	$1.461 \cdot 10^{10}$	0.037
	19.8	$1.12 \cdot 10^{-5}$	$9.81 \cdot 10^8$	2	2	570	0.73	$1.45 \cdot 10^6$	$3.13 \cdot 10^6$	0.073	0.203	$1.593 \cdot 10^{10}$	0.084
$1M_J$ 10 Gyr	20.0	$1.30 \cdot 10^{-5}$	$4.97 \cdot 10^8$	0.5	1	157	0.252	$2.01 \cdot 10^6$	$5.0 \cdot 10^6$	0.333	0.219	$1.89 \cdot 10^{10}$	0.024
	20.0	$1.30 \cdot 10^{-5}$	$4.97 \cdot 10^8$	2	1	532	1.11	$2.04 \cdot 10^6$	$3.30 \cdot 10^6$	0.062	0.250	$1.55 \cdot 10^{10}$	0.070
	20.0	$1.30 \cdot 10^{-5}$	$4.97 \cdot 10^8$	4	1	1100	1.77	$1.59 \cdot 10^6$	$3.18 \cdot 10^6$	0.0139	0.220	$1.63 \cdot 10^{10}$	3.87
	20.0	$1.30 \cdot 10^{-5}$	$4.97 \cdot 10^8$	0.5	0.5	368	0.634	$4.29 \cdot 10^6$	$1.87 \cdot 10^7$	0.088	0.271	$8.113 \cdot 10^{10}$	0.23
	20.0	$1.30 \cdot 10^{-5}$	$4.97 \cdot 10^8$	1	0.5	699	1.40	$4.78 \cdot 10^6$	$1.71 \cdot 10^7$	0.0456	0.281	$8.49 \cdot 10^{10}$	0.072
	20.0	$1.30 \cdot 10^{-5}$	$4.97 \cdot 10^8$	1	2	135	0.128	$5.13 \cdot 10^5$	$7.78 \cdot 10^5$	0.301	0.177	$3.14 \cdot 10^9$	0.0068
	20.0	$1.30 \cdot 10^{-5}$	$4.97 \cdot 10^8$	2	2	257	0.473	$8.8 \cdot 10^5$	$6.76 \cdot 10^5$	0.085	0.251	$3.36 \cdot 10^9$	0.069
$4M_J$ 0.5 Gyr	99.8	$8.37 \cdot 10^{-6}$	$6.50 \cdot 10^9$	1	1	1460	4.4	$7.28 \cdot 10^7$	$1.250 \cdot 10^8$	0.0058	0.374	$2.39 \cdot 10^{12}$	3.6
$4M_J$ 1 Gyr	97.9	$8.98 \cdot 10^{-5}$	$5.02 \cdot 10^9$	1	1	1130	3.3	$5.26 \cdot 10^7$	$8.47 \cdot 10^7$	0.00768	0.353	$1.542 \cdot 10^{12}$	0.63
$4M_J$ 10 Gyr	99.5	$1.06 \cdot 10^{-5}$	$2.42 \cdot 10^9$	1	1	554	1.1	$1.61 \cdot 10^7$	$2.48 \cdot 10^7$	0.0051	0.256	$3.28 \cdot 10^{11}$	0.054
$0.3M_J$ 5 Gyr	3.0	$3.61 \cdot 10^{-5}$	$3.18 \cdot 10^7$	1	1	213	0.48	$1.49 \cdot 10^5$	$8.3 \cdot 10^5$	0.030	0.28	$9.9 \cdot 10^8$	4.4
$0.7M_J$ 5 Gyr	19.6	$1.37 \cdot 10^{-5}$	$4.01 \cdot 10^8$	1	1	213	0.300	$1.41 \cdot 10^6$	$2.55 \cdot 10^6$	0.131	0.305	$5.31 \cdot 10^9$	0.033
$2M_J$ 5 Gyr	19.7	$1.12 \cdot 10^{-5}$	$1.24 \cdot 10^9$	1	1	1032	3.14	$1.03 \cdot 10^7$	$1.82 \cdot 10^7$	0.055	0.358	$2.26 \cdot 10^{11}$	0.90
$4M_J$ 5 Gyr	19.7	$1.08 \cdot 10^{-5}$	$2.49 \cdot 10^9$	1	1	2203	14.0	$3.57 \cdot 10^7$	$5.98 \cdot 10^7$	0.0041	0.526	$1.020 \cdot 10^{12}$	15